13 Large-Scale Structure and Baryon Oscillations

Hu Zhan, Wayne A. Barkhouse, James G. Bartlett, Sébastien Fromenteau, Eric Gawiser, Alan F. Heavens, Leopoldo Infante, Suzanne H. Jacoby, Christopher J. Miller, Jeffrey A. Newman, Ryan Scranton, Anthony Tyson, Licia Verde

13.1 Introduction

The six-band (*ugrizy*) LSST survey will yield a sample of ten billion galaxies (§ 3.7.2) over a huge volume. It will be the largest photometric galaxy sample of its time for studies of the large-scale structure of the Universe, and will characterize the distribution and evolution of matter on extragalactic scales through observations of baryonic matter at a broad range of wavelengths. In standard cosmology, structures on scales from galaxies to superclusters grow gravitationally from primordial adiabatic fluctuations that were modified by radiation and baryons between the Big Bang and recombination. Therefore, the large-scale structure encodes crucial information about the contents of the Universe, the origin of the fluctuations, and the cosmic expansion background in which the structures evolve.

In this Chapter, we focus on the potential of LSST to constrain cosmology with a subset of techniques that utilize various galaxy spatial correlations, counts of galaxy clusters, and cross correlation between galaxy overdensities and the cosmic microwave background (CMB) as described below. Chapter 14 describes the measurement of weak lensing with LSST, and in Chapter 15, we combine these with each other and other cosmological probes to break degeneracies and put the tightest possible constraints on cosmological models.

The shape of the galaxy two-point correlation function (or power spectrum in Fourier space) depends on that of the primordial fluctuations and imprints of radiation and baryons, which are well described by a small set of cosmological parameters (§ 13.2). Hence, one can constrain these parameters with the galaxy power spectrum after accounting for the galaxy clustering bias relative to the underlying dark matter. Of particular interest is the imprint on galaxy clustering of baryon acoustic oscillations (BAOs), which reflects the phases of acoustic waves at recombination as determined by their wavelengths and the sound horizon then ($\sim 100\,h^{-1}$Mpc). The BAO scales are sufficiently small that it is possible to measure them precisely with a large volume survey; yet, they are large enough that nonlinear evolution does not alter the scales appreciably. The BAO features can be used as a standard ruler to measure distances and constrain dark energy (§ 13.3). One can measure not only the auto-correlation of a galaxy sample but also cross-correlations between different samples (§ 9.5.4). The latter can provide valuable information about the redshift distribution of galaxies (see also § 3.8). The matter power spectrum on very large scales has not

been modified significantly by radiation or baryons, so it is one of the few handles we have on primordial fluctuations and inflation (§ 13.4). The bispectrum will arise from nonlinear evolution even if the perturbations are Gaussian initially. It contains cosmological information and can be used to constrain the galaxy bias (§ 13.5). The abundance of clusters as a function of mass and redshift is sensitive to cosmological parameters, and the required knowledge of the mass–observable relation and its dispersion may be achieved through multi-wavelength observations (§ 13.6, see also § 12.12). Finally, CMB photons traveling through a decaying potential well, such as an overdense region in the ΛCDM universe, will gain energy. In other words, the large-scale structure causes secondary anisotropies in the observed CMB. This effect can be measured from the correlation between galaxy overdensities and CMB temperature fluctuations, and it provides direct evidence for the existence of dark energy (§ 13.7).

13.2 Galaxy Power Spectra: Broadband Shape on Large Scales

Christopher J. Miller, Hu Zhan

The overall shape of the matter power spectrum is determined by the physical matter density, $\omega_{\rm m}$, the physical baryon density $\omega_{\rm b}$, the primordial spectral index, n_s, the running of the index, α_s, and neutrino mass, m_ν. For example, the prominent turnover at $k \sim 0.02\,h\,{\rm Mpc}^{-1}$ is related to the size of the particle horizon at matter–radiation equality and hence is determined by ω_m (and $T_{\rm CMB}$, which is precisely measured). The most significant component to the broadband shape of the power spectrum is this turnover, which has yet to be robustly detected in any galaxy survey. LSST provides the best opportunity to confirm this turnover and probe structure at the largest scales.

13.2.1 The Large Scale Structure Power Spectrum

For discrete Fourier modes, we define the three-dimensional power spectrum to be $P(k) \propto \langle|\hat{\delta}_k|^2\rangle$, where $\hat{\delta}_k$ is the Fourier transform of the density perturbation field, i.e., the overdensity, in a finite volume (see also Equation B.23 – Equation B.25). The choice of the underlying basis used to estimate the spatial power spectrum can be tailored to best suit the shape of the data; however, most work is expressed in the Fourier basis where the power spectrum is the Fourier inverse of the two-point spatial correlation function (Vogeley et al. 1992; Fisher et al. 1993; Park et al. 1994; da Costa et al. 1994; Retzlaff et al. 1998; Miller & Batuski 2001; Percival et al. 2001, 2007b). In the case of the CMB, we are accustomed to measuring the two-dimensional power spectrum, $C(\ell)$ of temperature fluctuations on the sky via spherical harmonics (e.g., Bond et al. 1998). The LSST survey will be studied using two-dimensional projections of the galaxy data as well (see § 13.3), but in this section we focus on the three-dimensional Fourier power spectrum.

Theoretical models for the shape of the power spectrum, which governs structure formation, start from the primordial $P_{pr}(k)$ spectrum. These primordial fluctuations are thought to have been generated during an inflationary period where the Universe's expansion was driven by a potential-dominated scalar field (e.g., Liddle & Lyth 2000). If this scalar field has a smooth potential, then $P_{pr}(k) \propto k^{n_{\rm s}}$ with $n_{\rm s} \sim 1$. However, it is possible that the scalar field was based on multiple or non-smooth potentials. Thus, determining the primordial power spectrum remains one of the

most important challenges for cosmology. In the specific case of a galaxy survey we measure the spectrum of galaxy density fluctuations, and relate this to the matter density fluctuations through a bias model, as described, e.g., in § 9.4.

Over time, the shape of the primordial power spectrum is modified by the effects of self-gravitation, pressure, dissipative processes, and the physical processes that determine the expansion rate; these effects take place on scales smaller than the horizon size at any given epoch. To account for these effects, the power spectrum is usually written as: $P(k,z) = T^2(k,z)P_{pr}(k)$, where $T(k,z)$ is the matter transfer function.

Calculating the transfer function involves solving the Boltzmann equation for all the constituents that play a role. For adiabatic models, the value of $T(k)$ approaches unity on large scales and decreases towards smaller scales. The degree of damping depends on the type of particles and processes. For instance, pure Cold Dark Matter (CDM) models produce less damping than Hot Dark Matter universes. Regardless of the species of matter, a turnover in the power spectrum will occur at the scale where pressure can effectively oppose gravity in the radiation-dominated era, halting the growth of perturbations on small scales. This bend in the shape of the power spectrum depends solely on the density of matter, $\omega_{\rm m}$, in the Universe and will be imprinted in the observed power spectrum.

Non-cosmological effects also change the shape of the observed power spectrum. The bias parameter between the dark matter and the galaxies will change the amplitude. While it is often assumed that bias is scale-independent (Scherrer & Weinberg 1998), there are observational (e.g., Percival et al. 2007b) and theoretical (§ 13.4.2) reasons to think otherwise. An unknown scale-dependent and stochastic bias will limit our ability to determine the matter power spectrum. The power spectrum of SDSS galaxies (Tegmark et al. 2004) is consistent with a bias independent of scale over $0.02\,{\rm Mpc}^{-1} < k < 0.1\,{\rm Mpc}^{-1}$, but the data are not terribly constraining, and there is room for subtle effects, which will become more apparent with better data. Extensive studies with the halo model, weak lensing, and simulations (Hoekstra et al. 2002; Hu & Jain 2004; Weinberg et al. 2004; Seljak et al. 2005b) will help us better understand the limits of galaxy bias. In this section, we assume that the bias is known and scale independent on scales of interest; see further discussion in § 13.5.

Any interactions between dark matter particles and baryonic matter will dampen the power at small scales (Miller et al. 2002), and photometric redshift errors will even suppress power on fairly large scales. In particular, in the presence of these errors, the observed power spectrum will become $P'(k) \propto P(k)\exp[-(k_{||}\sigma_z)^2]$, where $k_{||}$ are the modes parallel to the observer's line of sight and σ_z are the errors on the photometric redshifts (Seo & Eisenstein 2003). This damping will be large for scales smaller than 150 Mpc.

Thus while LSST's galaxy photometric redshift survey will be both very wide and very deep, the errors on these redshifts will greatly reduce its statistical power compared to spectroscopic surveys of the same size (e.g., Blake & Glazebrook 2003). Regardless of the challenges to measuring the power spectrum described here, LSST will provide the community with the largest view of our Universe in terms of the effective survey volume (see Figure 13.1), defined as

$$V_{\rm eff}(k) = \int \left[\frac{n_g(\boldsymbol{r})P'_g(k)}{n_g(\boldsymbol{r})P'_g(k)+1}\right]^2 d^3r, \tag{13.1}$$

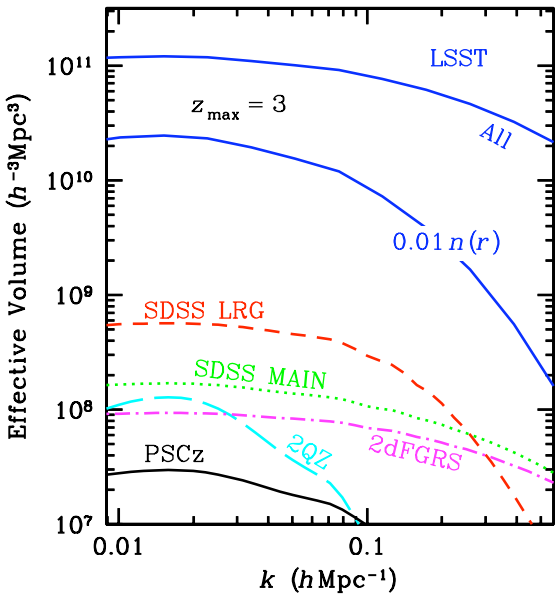

Figure 13.1: Effective survey volumes (see Equation 13.1). The survey data, except that of LSST, are from Eisenstein et al. (2005). LSST survey parameters are for the fiducial 20,000 deg^2 survey. The curve labeled with $0.01n(r)$ approximates the case where subvolumes or subsamples of LSST data are selected to explore systematic effects.

where $n_g(\boldsymbol{r})$ is the galaxy number density, and $P'_g(k)$ is the galaxy power spectrum in photometric redshift space.

13.2.2 Measuring the Turnover in the Power Spectrum for Photometric Redshift Surveys

In § 13.2.1, we discussed the various ways in which the observed power spectrum of galaxies differs from the true underlying dark matter power spectrum. In past and current galaxy surveys, the size and shape of the survey volume limited the largest scale for which power could be accurately measured. There is a minimum survey volume that is required to detect the turnover in the power spectrum, and LSST will be the first experiment to go well beyond that required size.

The shape and size of the survey volume affects the power spectrum by damping and smearing the power. Ideally, the survey volume would allow one to measure power in Fourier modes that are independent and uncorrelated between adjacent nodes. In practice, the size and shape of the volume puts limits on which nodes can be used in any analysis before severe window convolution and aliasing effects destroy the signal. In practice, the true underlying power spectrum, $P_{true}(k)$, is convolved with the survey window, $W(k)$:

$$\langle P_{windowed}(k)\rangle \propto \int |\hat{W}(\mathbf{k}-\mathbf{k}')|^2 P_{true}(\mathbf{k}')k'^2 dk'. \tag{13.2}$$

Figure 13.2 graphically describes these window effects for various modes within the LSST volume via the integrand of Equation 13.2, where we assume that the ratio of the observed power to the

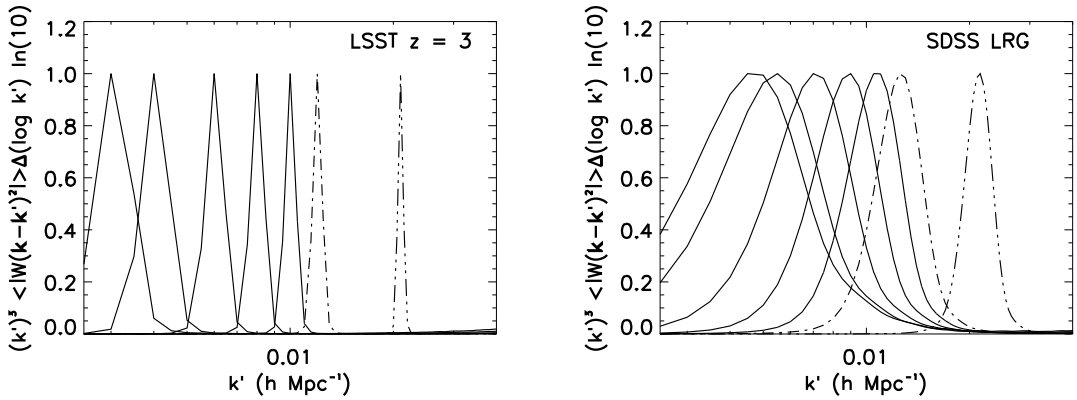

Figure 13.2: Measurement of the power spectrum at a given wavenumber invariably involves a window function, quantifying the range of values of k contributing (Lin et al. 1996). In a survey of infinite volume, the windows would be a series of δ functions. Shown are effective survey volume window functions for the LSST survey at $z = 3$ and the equivalent for the SDSS LRG sample. This is the integrand of Equation 13.2 multiplied by $k' ln 10 \Delta(log_{10} k')$ in this log-linear plot. The width and shape of the k-mode windows depend on the shape and size of the volume used for the Fourier analysis. The LSST windows are compact compared to the SDSS LRG windows. The LSST volume is large enough for the windows to provide uncorrelated measurements of the power spectrum to very large scales beyond the turnover (i.e., $k \sim 0.006\, h\,\mathrm{Mpc}^{-1}$). The window heights have been renormalized to emphasize the shapes and widths of adjacent windows.

true power is constant over the small k-range of each window (see Lin et al. 1996). The narrower the window, the cleaner the measurement. Indeed, the modes are essentially independent of one another and the survey volume window function biases the measurement little for $0.006\, h\,\mathrm{Mpc}^{-1} \leq k < 0.02\, h\,\mathrm{Mpc}^{-1}$, and for $k > 0.002\, h\,\mathrm{Mpc}^{-1}$, there is little or no "leakage" or aliasing of power into nearby bins. Compare with the SDSS LRG sample (Tegmark et al. 2006), where modes $k \leq 0.01\, h\,\mathrm{Mpc}^{-1}$ are strongly overlapping[1].

For shallow galaxy redshift surveys at low z, measuring $P(k)$ is straightforward. First, galaxy redshifts are converted to distances using the Hubble Law. The comoving density can then be determined. The power spectrum is then directly measured in Fourier space. The most significant challenge here is dealing with the window function, which describes the angular geometry of the survey. If the geometric basis used to estimate the power spectrum is not entirely orthogonal to the survey geometry, an effective window will distort the shape of the power spectrum and can even smear out sharp features like the baryon acoustic oscillations (e.g., Miller et al. 2002). From a statistical perspective, the problem here is that the power measured in any given wave-band becomes correlated with other wave-bands. This is not a significant issue for inferring the cosmological parameters, as one simply convolves the model power spectra with the same window during the analysis (e.g., Miller & Batuski 2001; Tegmark et al. 1998). This convolution comes at the expense of lost statistical power in the determination of the inferred parameters.

For deep photometric redshift surveys at high z, measuring $P(k)$ becomes more challenging. Arguably, if the window of a photometric survey like LSST is large and contiguous, then the window effects seen in many of the shallow low-redshift data sets (e.g., SDSS, the 2dF Survey) will not be

[1]Note this situation can be mitigated by using Karhunen-Loève eigenfunctions to find statistically independent modes (Szalay et al. 2003; Vogeley & Szalay 1996; Tegmark et al. 2004).

significant. However, the Hubble Law no longer suffices as a distance estimator. In addition, the evolution of the bias parameter (how light traces mass) and its dependence on scale also become issues. Last but not least, the photometric errors and their distributions affect the shape of the measured power spectrum.

Blake & Glazebrook (2003) and Seo & Eisenstein (2003) compare the power of redshift and photometric surveys to measure the power spectrum. They find that photometric surveys require 10 – 20 times more sky coverage than redshift surveys; there are fewer useful radial Fourier modes in photometric surveys because of the large errors in the photometric redshifts. On the other hand, Blake & Bridle (2005) show how the tangential modes, which are not affected by photometric redshift errors, can be used to provide good constraints on the large-scale shape of the large-scale structure power spectrum.

However, on the largest scales (i.e., comparable to the turnover scale), all Fourier modes can be used in the analysis. As an example from Blake & Bridle (2005), for a survey with $\sigma_0 = \sigma_z/(1+z) \sim 0.03$ (§ 3.8) with a survey volume effective depth corresponding to $z = 0.5$, all modes with $k < 0.02\,h\,\mathrm{Mpc}^{-1}$ will survive the damping caused by the use of photometric redshifts. They find the turnover at good statistical confidence (99.5%) for a photometric survey of 10,000 deg^2 to a limiting magnitude of $r = 24$. The LSST large-scale structure galaxy survey will have a much larger effective volume (due to its larger area and deeper magnitude limit) with photometric redshift errors comparable to $\sigma_0 \sim 0.03$ as used in Blake & Bridle (2005).

13.2.3 Other Systematics

In addition to the major systematics caused by the photometric redshifts, the large-scale structure power spectrum is also sensitive to effects such as star/galaxy misclassifications, dust extinction fluctuations on the sky, seeing fluctuations, color errors, which bias the photometric redshifts, and so on. In this section, we discuss how large these effects might be.

On very large scales, the variance of density fluctuations in logarithmic k bins is very small, e.g., $\Delta^2(k) \equiv k^3 P(k)/2\pi^2 \sim 10^{-3}$ at $k = 0.01\,\mathrm{Mpc}^{-1}$. An uncorrected-for varying Galactic extinction over the wide survey area can cause fluctuations in galaxy counts that may swamp the signal. If the logarithmic slope of galaxy counts $\bar{n}_\mathrm{g}(< m)$ as a function of magnitude is $s = \mathrm{d}\log\bar{n}_\mathrm{g}/\mathrm{d}m$, then the fractional error in galaxy counts is

$$\frac{\delta n_\mathrm{g}}{n_\mathrm{g}} = \ln 10\, s\, \delta m = 2.5\, s \frac{\delta f}{f}, \tag{13.3}$$

where $\delta f/f$ is the fractional error in flux caused by, e.g., extinction correction residuals. Observationally, s varies from 0.6 at blue wavelengths to 0.3 in the red (e.g., Tyson 1988; Pozzetti et al. 1998; Yasuda et al. 2001), and tends to be smaller for fainter galaxies (Metcalfe et al. 2001; Liske et al. 2003). To keep this systematic angular fluctuation well below $\Delta(k)$, one has to reduce the flux error to 1% or better over the whole survey area (thus motivating our requirements on photometric uniformity; see § 1.5). This is a very conservative estimate, because the power spectrum receives contributions from not only angular clustering but also radial clustering of galaxies on large scales, which is much less affected by extinction or photometry errors.

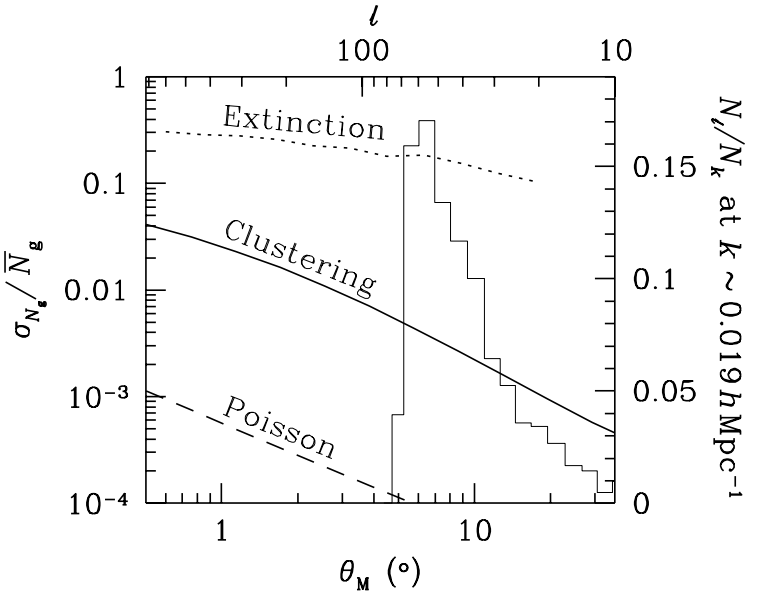

Figure 13.3: Rms fluctuations of galaxy counts on the sky due to the extinction (dotted line), galaxy clustering (solid line), and Poisson noise $1/\sqrt{\bar{N}_{\rm g}}$ (dashed line) within an angular window of size $\theta_{\rm M}$. The histogram shows the contribution to the number of independent modes, N_k ($k \sim 0.019\,{\rm Mpc}^{-1}$ with $\Delta k = 0.16k$), from each band of multipoles in the spherical harmonic analysis. The scale of the histogram is marked on the right axis. For lower wavebands, the distribution moves to lower multipoles. The multipole number, l, is related to $\theta_{\rm M}$ by $l \sim 360^{\rm o}/\theta_{\rm M}$. Figure from Zhan et al. (2006), with permission.

To understand how these effects might affect our measurements of galaxy fluctuations, we introduce some formalism from Zhan et al. (2006). The average number of galaxies within an angular window $\Theta(\hat{\mathbf{r}})$ is

$$\bar{N}_{\rm g} = \int \bar{n}_{\rm g}(r)\Theta(\hat{\mathbf{r}}){\rm d}^3 r, \tag{13.4}$$

and the variance is

$$\sigma^2_{N_{\rm g}} = \sum_{lm} \int P(k)|n_l(k)\Theta_{lm}|^2 k^2 {\rm d}k, \tag{13.5}$$

where $\bar{n}_g$ is the mean number density, $P(k)$ is the matter power spectrum at $z = 0$,

$$\begin{aligned} n_l(k) &= \sqrt{\frac{2}{\pi}} \int \bar{n}_{\rm g}(z) b(z) g(z) j_l(kr){\rm d}z, \\ \Theta_{lm} &= \int \Theta(\hat{\mathbf{r}}) Y^*_{lm}(\hat{\mathbf{r}}){\rm d}\hat{\mathbf{r}}, \end{aligned}$$

$b(z)$ is the linear galaxy bias, and $g(z)$ is the linear growth function of the large-scale structure. Since the scales of interest are very large, the linear approximation for the galaxy power spectrum is sufficient.

Zhan et al. (2006) use a Gaussian window function to demonstrate the effects:

$$\Theta(\theta, \phi) \equiv \Theta(\theta) = e^{-\theta^2/2\theta^2_{\rm M}},$$

where θ and ϕ are respectively the polar and azimuthal angles. For Galactic extinction, the Schlegel et al. (1998) map is used, and the Galactic latitude is restricted to $|b_c| > 20^o + 1.5\theta_M$. The rms fluctuation of g-band galaxy counts within the window function due to reddening alone is calculated with the conversion $\delta n_g/n_g \sim \delta A_B = 4.3\delta E(B-V)$.

The results are shown in Figure 13.3. The Galactic extinction (if it were not corrected for!) would dominate over galaxy clustering. However, we can 1) correct for the extinction to fairly high accuracy, using maps like that of Schlegel et al. (1998), and 2) use photometric redshifts to measure the clustering, thus greatly reducing the projection effects and increasing the true clustering signal. Analysis based on SDSS data demonstrates that the error caused by extinction (and photometry calibration) is an order of magnitude lower than the signal, the angular galaxy power spectrum, at multipoles of a few hundred (Tegmark et al. 2002). With better photometric calibrations (§ 2.6) and additional mapping of Galactic dust using the stellar locus (§ 7.5), LSST will be likely to reduce the error even further.

The rms fluctuations in projected galaxy number density due to large-scale structure is well under 1% on scales above several degrees, suggesting that the galaxy counts can be used to constrain photometric calibration drifts on these large scales. Further improvement on the relative flux error is possible by combining galaxy counts with multi-band galaxy photometry (e.g., Babbedge et al. 2005), HI and CO surveys, and stellar locus analyses (§ 7.5). An advantage of counting galaxies is that it does not rely on color information and, hence, is sensitive to gray dust. Since the Poisson noise in the galaxy counts is an order of magnitude lower than that caused by galaxy clustering, one can also divide the galaxies into groups of similar properties and compare them in one field with those in another to better determine the differential extinction.

13.3 Baryon Acoustic Oscillations

Hu Zhan

13.3.1 Introduction

Before the Universe became neutral for the first time at recombination, the cosmic plasma was tightly coupled with photons. Perturbations (acoustic waves) in the relativistic fluid propagated at the speed of sound ($v_s \sim c/\sqrt{3}$ for a relativistic fluid) but stopped after recombination when the fluid lost pressure support by the photons. The primary CMB temperature anisotropy is a snapshot of these acoustic waves at the last scattering surface, which can be characterized by the sound horizon, r_s ($\sim 100h^{-1}$Mpc co-moving), at that time (Peebles & Yu 1970; Bond & Efstathiou 1984; Holtzman 1989).

The low-redshift signature of the acoustic waves before recombination is a slight enhancement of the correlation between density fluctuations separated by a distance, r_s, and it is named after the source of the effect – Baryon Acoustic Oscillations (BAOs). Because there is only a single scale in effect, the acoustic peak can be easily identified in the two-point correlation function in configuration space (Eisenstein et al. 2005). In Fourier space, the imprint becomes a series of oscillations in the power spectrum at $k \sim 0.1h\,\mathrm{Mpc}^{-1}$. Since galaxies trace matter fairly well on large scales, and

since there is no known astrophysical process that can produce similar oscillatory features on the same scale, the BAO features must exist in the galaxy distribution as well. Indeed, they have been detected from SDSS and 2dF galaxy surveys, both spectroscopically and photometrically (Eisenstein et al. 2005; Cole et al. 2005; Padmanabhan et al. 2006; Blake et al. 2006; Percival et al. 2007a, 2009).

The scale of the BAO features shifts only slightly after recombination due to nonlinear evolution (e.g., Seo & Eisenstein 2005; Huff et al. 2007; Crocce & Scoccimarro 2008), which can be quantified by cosmological simulations (e.g., Seo et al. 2008). Hence, the BAO scale can be used as a CMB-calibrated standard ruler for measuring the angular diameter distance and for constraining cosmological parameters (Eisenstein, Hu, & Tegmark 1998; Cooray et al. 2001; Hu & Haiman 2003; Blake & Glazebrook 2003; Linder 2003; Seo & Eisenstein 2003; Wang 2006; Zhan 2006; Zhan, Knox, & Tyson 2009). Of particular interest are the dark energy equation of state and the mean curvature of the Universe.

LSST will observe $\sim 10^{10}$ galaxies over 20,000 deg^2 with redshifts estimated from its six-band photometry data. As we discussed in the previous section, the errors in the photometric redshifts (photometric redshifts) severely suppress the radial BAO information (Seo & Eisenstein 2003; Blake & Bridle 2005). Therefore, LSST will consider angular BAO only in redshift (or "tomographic") shells. With their superior photometric redshifts, supernovae should allow a full three-dimensional analysis; see the discussion in § 11.9.

Errors in photometric redshift cause bins in redshift to overlap in reality, giving rise to correlations between fluctuations of galaxy number density in adjacent bins. Such cross-bin correlations can be fairly strong when there is a significant overlap between two galaxy distributions, and, hence, provide useful information about the photometric redshift error distribution (see § 3.8). This is a crucial advantage of jointly analyzing galaxy and shear power spectra (see § 15.1).

For the science case presented here, we assume that by the time LSST is in full operation, we will have essentially perfect knowledge of the matter power spectrum at least in the quasi-linear regime (see § 15.5), so that we can sufficiently account for the slight evolution of the BAO features to achieve percent-level measurements of distances. We also assume that practical issues such as masks and angularly varying selection functions will be handled in such a way as to give systematic effects much smaller than the statistical errors of measured quantities. Finally, even though we adopt a very simple photometric redshift error model, we expect the results to be valid for a more realistic photometric redshift error distribution *if* the distribution can be modeled by a small number of parameters with high fidelity.

The rest of this section is organized as follows. § 13.3.2 describes the galaxy auto- and cross-power spectra in multipole space that will be measured by LSST. It also elaborates the assumed survey data and configuration for the forecasts. Treatment of photometric redshift errors is provided in § 13.3.3. Our estimates of constraints on distance, dark energy equation of state, and curvature are given in § 13.3.4. We demonstrate the constraining power of galaxy cross power spectra on the photometric redshift error distribution in § 13.3.5. We discuss limitations of the results, further work, and computational needs in § 13.3.6.

13.3.2 Galaxy Angular Power Spectra

As discussed in § 13.2 and § B.4.2, the power spectrum $P(k)$ completely characterizes the statistics of a Gaussian random field, which is a reasonable approximation for the cosmic density field on large scales, if primordial non-Gaussianity is negligible. With the Limber approximation (Limber 1954; Kaiser 1992), we project the three-dimensional matter power spectrum $\Delta^2_\delta(k)$ into angular power spectra $P(\ell)$ in multipole space

$$\begin{aligned} P_{ij}(\ell) &= \frac{2\pi^2}{c\ell^3}\int_0^\infty \mathrm{d}z\, H(z) D_\mathrm{A}(z) W_i(z) W_j(z) \Delta^2_\delta(k;z) + \delta^\mathrm{K}_{ij}\frac{1}{\bar{n}_i} \\ W_i(z) &= b(z) n_i(z)/\bar{n}_i, \end{aligned} \tag{13.6}$$

where subscripts correspond to different photometric redshift bins, $H(z)$ is the Hubble parameter, $D_\mathrm{A}(z)$ is the comoving angular diameter distance, $\Delta_\delta(k;z) = k^3P(k;z)/2\pi^2$, $k = \ell/D_\mathrm{A}(z)$, the mean surface density $\bar{n}_i$ is the total number of galaxies per steradian in bin i, δ^K_{ij} is the Kronecker delta function, and $b(z)$ is the linear galaxy clustering bias. (See § 9.5.4 for calculations of the two-point correlation function in configuration space.) The true redshift distribution of galaxies in the ith tomographic bin, $n_i(z)$, is an average of the underlying three-dimensional galaxy distribution over angles. It is sampled from an overall galaxy redshift distribution, $n(z)$, with a given photometric redshift model, as described in the next subsection. The last term in Equation 13.6 is the shot noise due to discrete sampling of the continuous density field with galaxies. The covariance between the power spectra $P_{ij}(\ell)$ and $P_{mn}(\ell)$ per angular mode is

$$C_{ij,mn}(\ell) = P_{im}(\ell)P_{jn}(\ell) + P_{in}(\ell)P_{jm}(\ell), \tag{13.7}$$

and the 1σ statistical error of $P_{ij}(\ell)$ is then

$$\sigma[P_{ij}(\ell)] = \left[\frac{P_{ii}(\ell)P_{jj}(\ell) + P^2_{ij}(\ell)}{f_\mathrm{sky}(2\ell+1)}\right]^{1/2}, \tag{13.8}$$

where $f_\mathrm{sky} = 0.485$, corresponding to the sky coverage of 20,000 deg^2.

For the forecasts in this section, we only include galaxy power spectra on largely linear scales, so that we can map the matter power spectrum to galaxy power spectrum with a scale-independent but time-evolving linear galaxy bias (Verde et al. 2002; Tegmark et al. 2004). Specifically, we require that the dimensionless power spectrum $\Delta^2_\delta(k;z) < 0.4$ in each tomographic bin. In addition, only multipoles in the range $40 \le \ell \le 3000$ are used. Very large-scale information is excluded here, but see § 13.4, § 13.7, and § 15.4 for its applications in testing non-standard models, such as primordial non-Gaussianity and dark energy clustering.

The linear galaxy bias assumes a fiducial model of $b(z) = 1 + 0.84z$, which is estimated from the simulation results in Weinberg et al. (2004). The exact value of $b(z)$ is not important for our purpose, though a higher bias does produce stronger signals (galaxy power spectra) and hence tighter parameter constraints. The dependence of the dark energy equation of state (w) error on the power spectrum amplitude can be found in Zhan (2006). We use CMBFAST version 4.5.1 (Zaldarriaga & Seljak 2000) to calculate the matter transfer function at $z = 0$, and then apply the linear growth function and Peacock & Dodds (1996) fitting formula to obtain the nonlinear matter

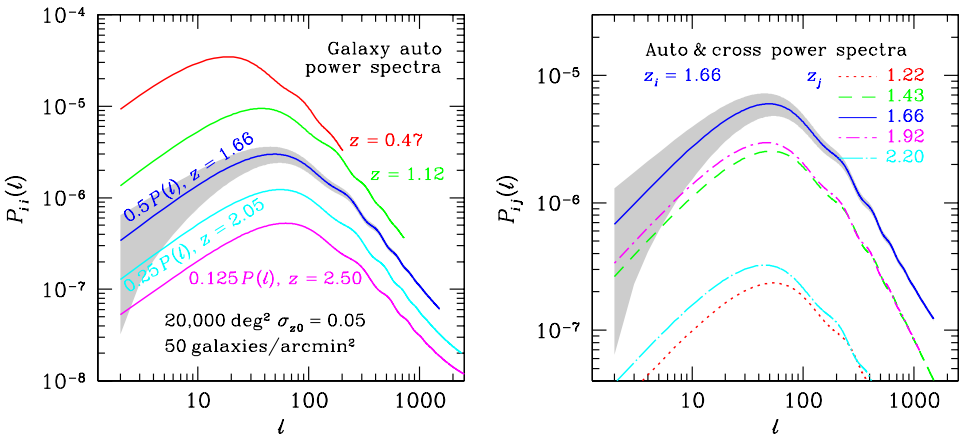

Figure 13.4: *Left panel*: Galaxy angular auto power spectra in five redshift bins (shifted for clarity). The central photometric redshift of each bin is as labeled, and the bin width is proportional to $1 + z$, increasing from 0.07 to 0.16 for the bins shown. We assume photometric redshift errors with rms $\sigma_z = 0.05(1 + z)$. The BAO features are prominent at multipole ℓ of several hundred. The gray area indicates the statistical error (cosmic variance and shot noise) *per multipole* for the bin centered at z = 1.66. Each power spectrum is shown to a value of ℓ beyond which nonlinear evolution would significantly contaminate our analysis. The flattening of the power spectra at $\ell \gtrsim 1000$, visible for the high-redshift curves, is due to shot noise. *Right panel*: Cross power spectra $P_{ij}(\ell)$ between bin i centered at $z = 1.66$ and bin j centered at $z = 1.22$ (4th neighbor, dotted line), 1.43 (2nd neighbor, dashed line), 1.66 (solid line), 1.92 (2nd neighbor, dash-dotted line), and 2.20 (4th neighbor, long-dash-dotted line). These quantify the effect of overlap between these bins, and can be used to quantify the photometric redshift error distribution.

power spectrum at any redshift. A direct application of the fitting formula to the CDM power spectrum would cause a large shift of the BAO features. In addition, it has difficulty processing power spectra that have an oscillating logarithmic slope (Zhan 2006). Thus, we calculate the multiplicative nonlinear correction to a linear matter power spectrum with no BAO features that otherwise matches the CDM power spectrum (Eisenstein & Hu 1999), and apply this ratio to the linear CDM power spectrum with BAO features (see also Eisenstein et al. 2005).

We assign LSST galaxies to 30 bins from photometric redshift of 0.15 to 3.5 with the bin width proportional to $1 + z$ in order to match the photometric redshift rms, $\sigma_z = 0.05(1 + z)$. The left panel of Figure 13.4 shows five auto power spectra labeled with their central photometric redshift. One can clearly identify the BAO features at multipole $\ell \gtrsim 100$ despite the radial averaging over the bin width. Note that the broadband turnover in Figure 13.4 between $\ell = 10$ and 100 does not directly correspond to the broadband turnover in the three-dimensional matter power spectrum $P(k)$. In full calculations without the Limber approximation, the angular power spectrum becomes flat on large scales (see, e.g., Loverde & Afshordi 2008). Since we exclude modes $\ell < 40$ and since smaller scale modes carry more statistical power, the errors of the Limber approximation on large scales have little impact on our results. The flattening of the $z = 2.05$ and 2.50 power spectra at $\ell \gtrsim 1000$ is due to the shot noise. However, this is not relevant, because the shot noise depends on binning (hence, $\bar{n}_i$); what is relevant is the amount of information that can be extracted with a particular binning scheme (see Zhan 2006).

The right panel of Figure 13.4 shows four cross power spectra between the bin centered on $z = 1.66$ and its neighbors. The auto spectrum at $z = 1.66$ is included for reference. The amplitude of the cross power spectrum is largely determined by the overlap between the two bins in true redshift

space, so it decreases rapidly with the bin separation (given our Gaussian photometric redshift model). The cross-bin power spectra can be used to self-calibrate the photometric redshift error distribution (see also § 3.8.5 and § 9.5.4).

13.3.3 Photometric Redshift Treatment

We assume that the photometric redshift error distribution follows a truncated Gaussian:

$$\mathcal{P}(z_{\rm p};z) \propto \begin{cases} \exp\left[-\frac{(z_{\rm p}-z-\delta z)^2}{2\sigma_z^2}\right] & z_{\rm p} \geq 0 \\ 0 & z_{\rm p} < 0, \end{cases} \tag{13.9}$$

where the subscript p signifies photometric redshifts, δz is the photometric redshift bias, and σ_z is the photometric redshift rms error. Since any photometric redshift bias known a priori can be taken out, one can set the fiducial value $\delta z = 0$ and allow it to float. For the rms, we adopt the fiducial model $\sigma_z = \sigma_{z0}(1+z)$ with $\sigma_{z0} = 0.05$. The truncation in Equation 13.9 implies that galaxies with negative photometric redshifts have been discarded from the sample, which is not essential to our analysis. The photometric redshift bias and rms error at an arbitrary redshift are linearly interpolated from 30 photometric redshift bias, δz_i, and rms, σ_{zi}, parameters evenly spaced between $z = 0$ and 4 (Ma, Hu, & Huterer 2006; Zhan 2006); they are linearly extrapolated from the last two rms and bias parameters between $z = 4$ and 5, beyond which we assume practically no galaxy in the sample. We describe in § 13.3.5 how we might constrain these quantities. Note that the photometric redshift parameters are assigned in true-redshift space independent of galaxy bins, which are specified in photometric redshift space.

The underlying galaxy redshift distribution can be characterized by (Wittman et al. 2000)

$$n(z) \propto z^\alpha \exp\left[-(z/z^*)^\beta\right] \tag{13.10}$$

with $\alpha = 2$, $z^* = 0.5$, $\beta = 1$, and a projected galaxy number density of $n_{\rm tot} = 50$ per square arc-minute for LSST (see § 3.7.2). This distribution peaks at $z = 1$ with approximately 10% of the galaxies at $z > 2.5$. The galaxy distribution $n_i(z)$ in the ith bin is sampled from $n(z)$ by (Ma et al. 2006; Zhan 2006)

$$n_i(z) = n(z)\mathcal{P}(z_{p,i}^{\rm B}, z_{p,i}^{\rm E}; z), \tag{13.11}$$

where $z_{p,i}^{\rm B}$ and $z_{p,i}^{\rm E}$ define the extent of bin i, and $\mathcal{P}(a,b;z)$ is the probability of assigning a galaxy that is at true redshift z to the photometric redshift bin between $z_p = a$ and b. With Equation 13.9, the probability becomes

$$\begin{aligned} \mathcal{P}(z_{p,i}^{\rm B}, z_{p,i}^{\rm E}; z) &= I(z_{p,i}^{\rm B}, z_{p,i}^{\rm E}; z)/I(0,\infty;z), \\ I(a,b;z) &= \frac{1}{\sqrt{2\pi}\,\sigma_z}\int_a^b dz_p \exp\left[-\frac{(z_p-z-\delta z)^2}{2\sigma_z^2}\right]. \end{aligned}$$

We have discarded the possibility of negative photometric redshifts here by normalizing the probability with $I(0,\infty;z)$. It is worth mentioning that even though the probability distribution of photometric redshifts at a given true redshift is assumed Gaussian, the reverse is not true. In other words, the Gaussian assumption is flexible enough to allow for modeling of more complex galaxy distributions in tomographic bins (Ma et al. 2006).

13.3.4 Constraints on Distance, Dark Energy, and Curvature

We apply the Fisher matrix analysis (e.g., Tegmark 1997, see § B.4.2 for details) to estimate the precisions LSST BAO can achieve on distance, dark energy, and curvature parameters. This involves two separate calculations: 1) estimating the constraints on distance (and growth) parameters with a set of cosmological and nuisance parameters that are modified to have no effect on distance (or growth of the large-scale structure), and 2) estimating the constraints on the set of cosmological and nuisance parameters specified in Appendix A and previous subsections. The latter can be done by a projection of the results of the former. We give a brief account here; a full discussion of the subtle details is given in Zhan et al. (2009).

We assign 14 co-moving distance parameters D_i ($i = 1 \ldots 14$) at redshifts evenly spaced in $\log(1+z)$ from $z_1 = 0.14$ to $z_{14} = 5$[2]. For the BAO measurement, we'll need the standard angular diameter distance. But for the weak lensing analysis (Chapter 14), we will find it useful to define the more general co-moving angular diameter distance $D_A(z, z')$ of z' as viewed from z. This quantity is related to the co-moving radial distance $D(z, z')$ between z' and z via

$$D_A(z,z') = \begin{cases} K^{-1/2}\sin[D(z,z')K^{1/2}] & K > 0 \\ D(z,z') & K = 0 \\ |K|^{-1/2}\sinh[D(z,z')|K|^{1/2}] & K < 0 \end{cases}, \tag{13.12}$$

where the curvature $K = -\Omega'_{\rm k}(H_0/c)^2$. Since the co-moving distance is interpolated from the distance parameters, the curvature parameter has no effect on distance except through Equation 13.12. Hence, we label it as $\Omega'_{\rm k}$ to distinguish from the real curvature parameter $\Omega_{\rm k}$.

Constraints on $\Omega'_{\rm k}$ will hold for any model that preserves the Friedmann-Robertson-Walker metric and (the form of) Equation 13.6, whereas curvature constraints from exploiting the full functional dependence of the angular diameter distance or luminosity distance on $\Omega_{\rm k}$ (e.g., Knox, Song, & Zhan 2006; Spergel et al. 2007) are valid only for a particular cosmological model. For this reason, measurements of $\Omega'_{\rm k}$ are considered pure metric tests for curvature (Bernstein 2006). However, because BAO (or weak lensing) alone does not constrain $\Omega'_{\rm k}$ (Bernstein 2006; Zhan et al. 2009), we defer further discussion until § 15.1 where joint analyses of multiple techniques are presented.

The left panel of Figure 13.5 demonstrates that LSST BAO can achieve percent level precision on nine co-moving distances between $z = 0.29$ and 3.1 with WMAP five-year priors (Komatsu et al. 2009, solid line). Stronger priors from Planck will further reduce the errors to $\sim 0.5\%$ (open circles). The results include an additive noise power of 10^{-8} per galaxy bin. The galaxy bias and growth parameters are allowed to float freely. We have applied fairly weak priors to the photometric redshift parameters described at the beginning of the previous subsection: $\sigma_P(\delta z) = 2^{-1/2}\sigma_P(\sigma_z) = 0.2\sigma_z$, which would take only 25 galaxy spectra for calibration around each photometric redshift bias parameter (and given the spacing of these parameters, this corresponds to 188 spectra per unit redshift) in the Gaussian case.

[2]The actual calculation is done with 15 Hubble parameters H_i ($i = 0, \ldots, 14$) and then projected into D_i ($i = 1, \ldots, 14$ and H_0 unchanged) for reasons stated in Zhan et al. (2009). We include 15 growth parameters as well, but the growth measurements contribute little to the cosmological constraints in this section.

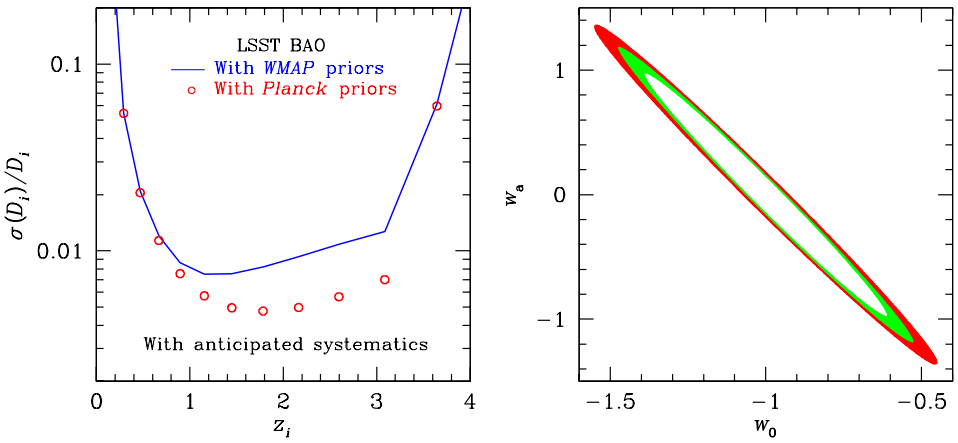

Figure 13.5: *Left panel*: Marginalized 1-σ errors on the co-moving distance from LSST angular BAO measurements. We have assumed that the photometric redshift bias δz_i is known within $\pm 0.2\sigma_{z,i}$, or $\sigma_P(\delta z_i) = 0.01(1+z_i)$, per redshift interval of ~ 0.13 from independent sources. For Gaussian photometric redshift errors, this prior on δz_i would mean a calibration sample of 188 galaxy spectra per unit redshift. Figure from Zhan et al. (2009), with permission. *Right panel*: Marginalized 1-σ error contours of the dark energy equation of state parameters w_0 and w_a. The innermost contour assumes that the linear galaxy clustering bias b_i is known within 15% and that $\sigma_P(\delta z_i) = 0.05\sigma_{z,i}$, i.e., 3000 spectra per unit redshift for calibration in the Gaussian case. The outer contour of the green shaded area corresponds to no prior on the galaxy bias [for numerical reasons, we take $\sigma_P(\ln b_i) = 1000$] and $\sigma_P(\delta z_i) = 0.05\sigma_{z,i}$. The outermost contour further relaxes $\sigma_P(\delta z_i)$ to $0.4\sigma_{z,i}$. To reduce the number of parameters that are varied, we peg the uncertainty in the photometric redshift rms to $\sigma_P(\sigma_{z,i}) = \sqrt{2}\sigma_P(\delta z_i)$ in both panels.

The right panel of Figure 13.5 shows error contours of the dark energy equation of state parameters, w_0 and w_a, with different priors on the galaxy bias b and photometric redshift parameters. The innermost contour assumes $\sigma_P(b)/b = 15\%$, which is aggressive but comparable to current determination for low redshift galaxies (Hoekstra et al. 2002; Verde et al. 2002; Seljak et al. 2005a), and $\sigma_P(\delta z) = 2^{-1/2}\sigma_P(\sigma_z) = 0.05\sigma_z$, i.e., 400 spectra for calibration around each photometric redshift bias parameter in the Gaussian case. The intermediate contour allows the galaxy bias parameters to float freely while keeping the same photometric redshift priors. The outermost contour also allows b to float freely but relaxes the photometric redshift priors to $\sigma_P(\delta z) = 2^{-1/2}\sigma_P(\sigma_z) = 0.4\sigma_z$. It is not surprising that the LSST BAO constraints on w_0 and w_a change only mildly with wild variations in the priors, because the distances are determined from the BAO features in the galaxy angular power spectra not from the amplitudes and because the cross-bin power spectra can self-calibrate the photometric redshift error distribution.

The curvature constraint depends on the parametrization of the dark energy equation of state. With the equation of state parametrized as $w(a) = w_0 + w_a(1-a)$, LSST BAO can achieve $\sigma(\Omega_k) \sim 10^{-3}$ (Zhan 2006; Knox et al. 2006). This is an order of magnitude improvement over the current result with the assumption of a constant equation of state (e.g., Spergel et al. 2007).

13.3.5 Constraining Photometric Redshift Parameters

§ 3.8 discusses direct methods for determining galaxy photometric redshifts, including calibration of the photometric redshift error distribution using cross-correlations between the photometric redshift sample and a spatially overlapping spectroscopic sample (Newman 2008). Here we present

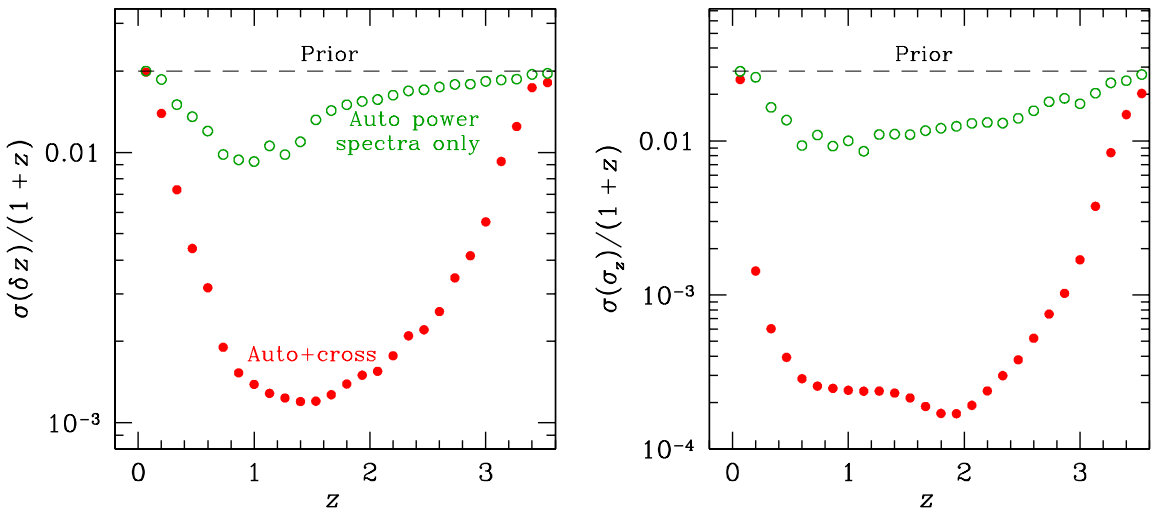

Figure 13.6: *Left panel*: Marginalized 1σ constraints on the photometric redshift bias parameters from the galaxy auto power spectra (open circles) and full set of galaxy auto and cross power spectra (filed circles). The thin dashed line marks the imposed weak prior $\sigma_P(\delta z_i) = 0.4\sigma_{z,i} = 0.02(1+z_i)$. The cross power spectra can self-calibrate the photometric redshift bias to 10^{-3} level, which is very useful for weak lensing. *Right panel*: Same as the left panel but for the photometric redshift rms parameters.

another method to calibrate the photometric redshift error distribution using cross-power spectra between photometric redshift samples themselves (Zhan 2006; Schneider et al. 2006). Even bins that don't overlap in photometric redshift will overlap in true redshift and, therefore, include galaxies that are physically correlated with one another. Figure 13.6 shows marginalized 1σ constraints on the photometric redshift bias (left panel) and rms[3] (right panel) parameters corresponding to the outermost contour in the right panel of Figure 13.5. Results of using only the auto power spectra are shown in open circles (which are statistically incorrect because the correlations between the bins – the cross power spectra – have been neglected), and those from the full set of power spectra are in filled circles. The thin dashed line in each panel represents the priors. It is remarkable that the cross-bin power spectra can place such tight constraints on the photometric redshift parameters. This explains why the dark energy constraints in Figure 13.5 are not very sensitive to the photometric redshift priors. Moreover, as we discuss in § 15.1, the capability of self-calibrating the photometric redshift error distribution with galaxy power spectra is a crucial advantage for combining BAO with weak lensing over the same data. However, we emphasize as well that the BAO self-calibration of the photometric redshift parameters cannot replace spectroscopic calibrations, because without knowing how to faithfully parametrize the photometric redshift error distribution, the self-calibration will be less informative.

[3]The smallest errors of the rms occur at $z \sim 1.9$ where the galaxy bin widths match the photometric redshift parameter spacing of $\Delta z = 0.13$. We have replaced the uniform sampling of the galaxy distribution $n_i(z)$ in Zhan (2006) by an adaptive sampling to improve the accuracy of the tails of $n_i(z)$. This, in turn, leads to tighter constraints on σ_z in Figure 13.6 than those in Zhan (2006), adjusted for different number of parameters and number of galaxy bins.

13.3.6 Discussion

Photometric redshift errors are one of the most critical systematics for an imaging survey, as redshift errors directly affect the interpretation of the distance–redshift and growth–redshift relations, from which constraints on dark energy and other cosmological parameters are derived. Even though the galaxy cross power spectra can self-calibrate the parameters of a Gaussian photometric redshift error model, such capability must be quantified for realistic photometric redshift errors. Another method of calibrating the photometric redshift error distribution is to cross-correlate the photometric redshift sample with a spatially overlapping spectroscopic sample (Newman 2008, see § 3.8), which does not have to be as deep as the photometric redshift sample. These indirect methods hold promise for application to future surveys, though it is also noted that lensing by foreground galaxies can produce spurious cross-correlations and contaminate the results (Loverde, Hui, & Gaztañaga 2008; Bernstein & Huterer 2009).

The Limber approximation is accurate only when the width of the redshift bin is much larger than the linear size corresponding to the angular scale of interest (Limber 1954; Kaiser 1992). In other words, the angular power spectra calculated using Equation 13.6 are not accurate on large scales (low ℓs) (e.g., Loverde & Afshordi 2008). Since we do not use multipoles $\ell < 40$, the impact on our results is small. Nevertheless, the inaccuracy of the Limber approximation is not necessarily a loss of information, but one should do the full calculation without the approximation if low multipoles are included in the parameter estimation. Similarly, one should model the correlations induced by lensing (Loverde et al. 2008) based on the foreground galaxy distribution.

The two-point correlations in configuration space are calculated by counting pairs and hence scale with N^2, where N is the number of objects. With a hierarchical algorithm, the computational cost can be reduced to $N \log N$. In Fourier space, the power spectrum calculation scales as $N \log N$ with Fast Fourier Transforms. The advantage of working in Fourier space is that the errors of the modes are independent of each other, but one has to deconvolve unavoidable masks and anisotropic selection function to obtain the true power spectra, which can give rise to correlations between the modes.

13.4 Primordial Fluctuations and Constraints on Inflation

Licia Verde, Hu Zhan

Very large-scale fluctuations in the matter distribution entered the horizon after the epoch of matter–radiation equality and grew primarily under gravity since then. Therefore, these fluctuations preserve the imprint of primordial quantum perturbations. This provides a handle on models of inflation. More specifically, the overall shape of the primordial matter power spectrum, as described by the primordial spectral index and its running, is controlled by inflationary slow-roll parameters, which also determine the shape of the inflation potential. Furthermore, any departure from the approximately featureless power law or non-Gaussianity detected on very large scales will require some detailed modeling in the context of inflation. Of course, other causes such as dark energy clustering are equally interesting to explore.

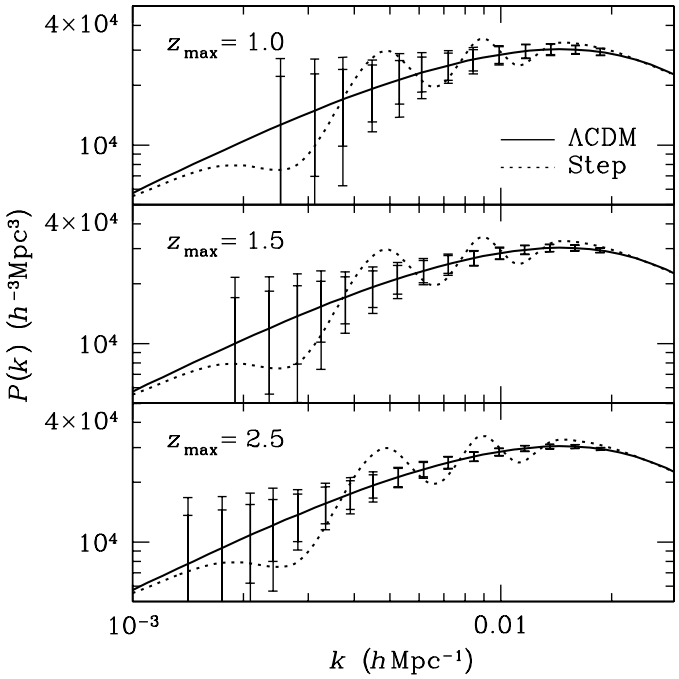

Figure 13.7: Effect of depth (z_{max}) on error forecasts for measurements of the matter power spectrum with LSST (Zhan et al. 2006). A 20,000 deg^2 photometric galaxy redshift survey is assumed. The solid line is the fiducial model power spectrum, while the dotted line is the power spectrum generated by the step inflation potential (Peiris et al. 2003). The error bars are 1σ statistical errors of the power spectrum measured in non-overlapping logarithmic bins with bin width $\Delta k \sim 0.16k$. The inner error bars are based on simple mode-counting in a cubic volume, while the outer ones count spherical harmonic modes. All the power spectra are scaled to $z = 0$. Figure from Zhan et al. (2006), with permission.

13.4.1 Features in the Inflation

Features in the inflation can generate features in the primordial spectrum of perturbations that make it deviate from a simple power law. For example, it can induce features such as a step or a bump, which should then be detectable in the CMB power spectrum and in the galaxy power spectrum. Figure 13.7 illustrates that a step inflation potential consistent with *WMAP* three-year data (Peiris et al. 2003) induces oscillations in $P(k)$ that can be detected by the full ten-year LSST survey (Zhan et al. 2006).

On scales larger than $k \sim 0.05\,\mathrm{Mpc}^{-1}$, CMB data are already cosmic variance dominated. A deep and wide photometric redshift galaxy survey such as LSST can provide measurements on these scales with comparable errors. Moreover, those features should be more pronounced in the three-dimensional matter power spectrum (even with photometric redshift errors) than in the projected two-dimensional CMB temperature power spectrum. Figure 13.8 demonstrates that the estimated statistical errors of the primordial power spectrum from LSST (Zhan et al. 2006) are competitive with those from the CMB (Hu & Okamoto 2004). Hence, the addition of large-scale structure data will significantly improve our knowledge about the primordial fluctuations.

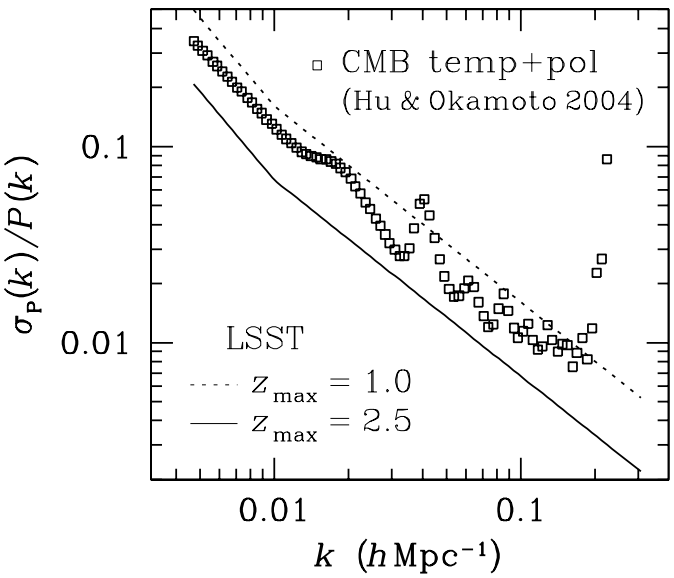

Figure 13.8: Forecasts of sample variance errors on the primordial matter power spectrum (Zhan et al. 2006). For the LSST, we set $z_{\rm max} = 1.0$ (dotted line) and 2.5 (solid line). The forecast for the CMB (open squares) includes both temperature and polarization information, and it is taken from Hu & Okamoto (2004). Both forecasts assume a binning of $\Delta k = 0.05k$. Figure from Zhan et al. (2006), with permission.

13.4.2 Non-Gaussianity from Halo Bias

Dalal et al. (2008) and Matarrese & Verde (2008) have shown that primordial non-Gaussianity affects the clustering of dark matter halos, inducing a scale-dependent bias, arising even for Gaussian initial conditions. The workhorse non-Gaussian model is the so-called local model: $\Phi = \phi + f_{NL}(\phi^2 - \langle\phi^2\rangle)$ where ϕ denotes a Gaussian random field, Φ denotes the Bardeen potential (which on sub-horizon scales reduces to the negative of the gravitational potential), and f_{NL} is the non-Gaussian parameter. Local non-Gaussianity arises in inflationary models where the density perturbations are created outside the horizon and can have a large f_{NL} in models like the curvation or in multi-field inflation. In this case, the non-Gaussian correction $\Delta b^{F_{NL}}$, to the standard halo bias increases as $\sim 1/k^2$ at large scales and roughly as $(1+z)$ as function of redshift. Galaxy surveys can be used to detect this effect, which would appear as a difference between the shape of the observed power spectrum on large scales, and that expected for the dark matter. The signature of non-Gaussianity is a smooth feature, thus photometric surveys are well suited to study this effect. Carbone et al. (2008) estimate that LSST would yield a 1-σ error on $f_{NL} \lesssim 1$. Figure 13.9 illustrates the effect of the large-scale non-Gaussian bias. This error could be in principle reduced further if cosmic variance could be reduced (see Seljak 2009; Slosar 2009). In any case this limit of $\sigma(f_{NL}) \lesssim 1$ is particularly interesting for two reasons: 1) it is comparable to, if not better than, the limit achievable from an ideal CMB experiment, making this approach highly complementary to the CMB approach and 2) inflationary models such as curvation or multi-fields can yield f_{NL} as large as ~ 10, while f_{NL} from standard slow-roll inflation is expected to be $\ll 1$; a constraint of $\sigma(f_{NL}) \lesssim 1$ from LSST can be a useful test for these inflationary models.

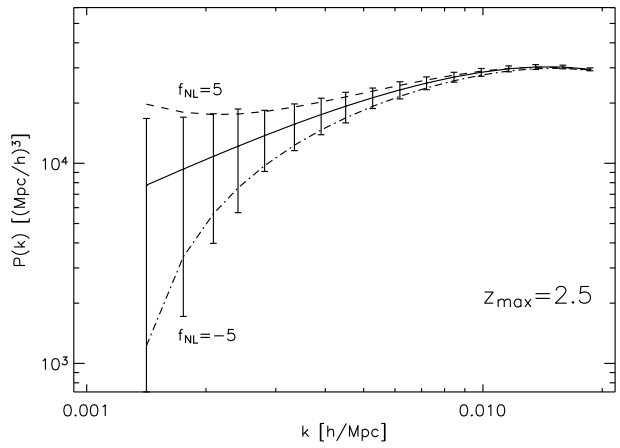

Figure 13.9: Effect on the large scale observed galaxy power spectrum of a primordial non-Gaussianity of the local type described by an f_{NL} parameter of the values ± 5. Such departure from Gaussian initial conditions can be detected at the level of several σ by LSST, while the CMB Planck experiment is expected to have an error bound of $\sigma(f_{NL}) = 5$. While the simplest, single field, slow-roll inflation models predict $f_{NL} < 1$, several models (multi-field models, non-slow roll models) yield much larger deviations from Gaussianity, which would be detectable with LSST. We have adopted the same conventions as in Figure 13.7.

13.5 Galaxy Bispectrum: Non-Gaussianity, Nonlinear Evolution, and Galaxy Bias

Licia Verde, Alan F. Heavens

The classic paper of Kaiser (1984) suggested that galaxies form at high peaks of the dark matter distribution, and are thus *biased* tracers of the mass distribution (§ 9.4). There are many theoretical models for galaxy bias, and observations have shown that it depends on galaxy type, redshift, and possibly scale (e.g., Swanson et al. 2008; Blanton et al. 2006; Zehavi et al. 2005; Mo et al. 1997; Cresswell & Percival 2009; Norberg et al. 2001). However to a good approximation (and ignoring the effects of *primordial* non-Gaussianity described above), on large scales the effect of bias can be summarized as

$$P_g = b^2 P_{DM}, \tag{13.13}$$

where P_g denotes the galaxy power spectrum, P_{DM} denotes the underlying dark matter power spectrum, and b denotes the bias parameter. The *relative* bias of galaxies is relatively straightforward to measure using the power spectrum or two-point function of galaxy clustering split by type (§ 9.5.4), but the absolute bias is more difficult to establish. It can be measured from the observed galaxy power spectrum, given predictions for the underlying clustering of dark matter given our concordance cosmological model (e.g., Lahav et al. 2002). However, if we had an independent measurement of the bias factor, we could combine CMB and galaxy clustering measurements to make more precise measurements of cosmological parameters and the growth rate of large-scale structure under gravity. In linear theory one cannot use measurements of large-scale structure to distinguish between bias and the growth rate of structure. However, to second order, the degeneracy is lifted (Fry 1994). The second-order corrections depend on the gravitational clustering of dark matter, and one can determine the bias factor by measuring the shape dependence of the

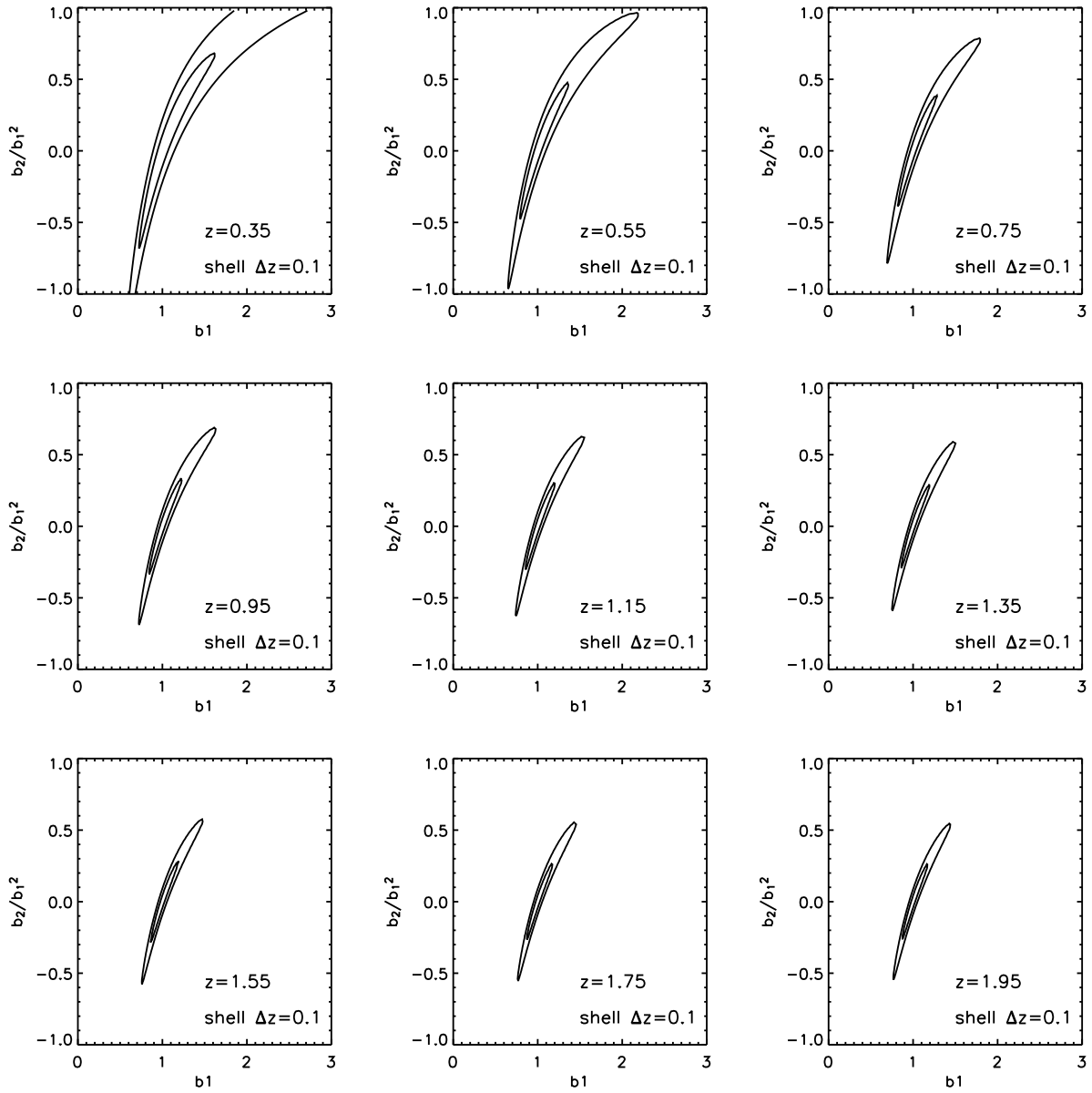

Figure 13.10: Predicted $1\,\sigma$ and $2\,\sigma$ uncertainties on the first- and second-order bias parameter as measured from the bispectrum of galaxies in redshift shells. Only alternate redshift bins are shown to illustrate the scaling of the errors with redshift.

three-point correlation function (or its Fourier analogue, the bispectrum). Indeed, going to second order in perturbation theory suggests going to second order in the bias model, and we parametrize bias as:

$$\delta(\mathbf{r})_{galaxies} = b_1\delta(\mathbf{r})_{DM} + b_2\left(\delta^2(\mathbf{r})_{DM} - \left\langle\delta^2_{DM}\right\rangle\right). \tag{13.14}$$

The Fry (1994) approach allows both b_1 and b_2 to be determined. While primordial perturbations are expected to be Gaussian (§ 13.4), the observed galaxy distribution is non-Gaussian for two reasons: 1) non-linear gravitational instability introduces a skewness in the density distribution and thus non-Gaussianity and 2) the non-linear bias of Equation 13.14 also skews the distribution.

The bispectrum approach has been applied successfully to spectroscopic surveys to measure bias (e.g., Verde et al. 2002). Photometric redshift errors will not allow us to use any radial clustering information in the LSST data on the mildly nonlinear scales of relevance. Verde et al. (2000) computed the expected errors on the bias parameters for a photometric survey with the depth of APM ($r \sim 20$). We scale these results to LSST as follows: 1) we can use photometric redshifts to divide the LSST sample in shells of width $\Delta z = 0.1$ yielding negligible cross-correlation between shells; 2) in each of these shells we compute how many volumes of the Verde et al. (2000) set-up will fit within the volume, and rescale the errors accordingly; 3) we assume that the shot noise level is similar to that of Verde et al. (2000); 4) we conservatively assume that in all shells perturbation theory breaks down at the same scales as it does at $z < 0.1$; and 5) we assume the effects of bias evolution and growth factor with redshift cancel. The resulting predicted uncertainties in b_1 and b_2 are shown in Figure 13.10 for a few redshift slices. In the figure $b_1 = b_{linear} \times G(z)$, where $G(z)$ is the linear growth factor.

We can do better if we assume a functional form for the evolution of bias. For example, for a one-parameter toy model where $b_{linear}(z) = b_1/G(z)$, the constraint on b_1 (marginalized over b_2), we estimate $1\,\sigma$ and $2\,\sigma$ errors on b_1 of 0.045 and 0.1 respectively.

13.6 The LSST Cluster Sample

James G. Bartlett, Wayne A. Barkhouse, Sébastien Fromenteau, Licia Verde, Jeffrey A. Newman

The number density of clusters as a function of redshift depends on the rate at which cosmic structures grow; it also depends on the cosmic volume element as a function of redshift. It, therefore, probes both dynamical and geometrical aspects of the cosmological model as a function of redshift. This is a powerful combination for discovering the nature of dark energy and any deviations from standard gravity (see also § 12.12), as emphasized, for example, by the Dark Energy Task Force (Albrecht et al. 2006, 2009).

The method relies on our ability to accurately predict cluster abundance and its evolution as a function of observable cluster properties and of the cosmological parameters. The feasibility of this, in turn, rests on connecting observable cluster properties to those of the host dark matter halos. N-body simulations then robustly provide the halo abundance function, often fit by simple analytical forms (Press & Schechter 1974; Sheth et al. 2001; Jenkins et al. 2001).

The critical link is the relationship between observable quantities of clusters, and the properties of the halos in which clusters live. Fortunately, clusters obey a number of simple *scaling relations*

between cluster observables themselves, on the one hand, and halo mass and redshift on the other. In other words, there is a one–to–one relation (albeit with scatter) between a cluster and its host halo governed by well–defined correlations. This differs significantly from the case of a typical galaxy, which does not on average identify with an individual dark matter halo.

We can, therefore, view clusters as dark matter halos "tagged" with different observational signatures: a grouping of galaxies in physical and color space; X–ray emission from the hot intracluster medium; the Sunyaev–Zel'dovich (SZ) signal in the Cosmic Microwave Background caused by the same hot gas; and peaks in gravitational shear maps (§ 14.3.8). The existence of many different observational signatures plays an important role in identifying and controlling cluster modeling and corresponding systematic effects in cosmological analyses.

As we discuss in this section, LSST will produce a large catalog of clusters detected through their member galaxy population out to and beyond redshift unity. This catalog will on its own enable an important cosmological study of dark energy and gravity. Moreover, a number of wide–area cluster surveys in other wavebands will also have produced catalogs in the LSST era, including the SPT SZ survey (Ruhl et al. 2004; Staniszewski et al. 2008) over several thousand deg^2, the Planck all–sky SZ [4] survey and an all–sky X–ray survey from eROSITA[5].

For all of these, LSST will identify optical counterparts and provide deep optical–band imaging. The resulting host of multi–band catalogs will be highly valuable for two reasons: Firstly, the comparison of catalogs in different wavebands will allow us to ferret out systematics related to cluster detection and will tighten the modeling of survey selection functions. Secondly, the deep imaging will allow us to calibrate the cluster observables–mass distribution function through gravitational lensing measures of cluster mass (§ 12.12, where the use of clusters to constrain cosmological parameters is discussed).

13.6.1 The Method

In this section we describe implementation of the cluster counting method in detail. We keep the discussion general to serve as a reference not only to analysis of LSST's own cluster catalog, but also to the improvements LSST will bring in its application to catalogs at other wavebands.

We may usefully break the method down into three main steps:

1. Catalog construction
2. Mass determination
3. Cosmological analysis

At the heart of catalog construction is the cluster detection algorithm, which determines the catalog selection function (*completeness*) and *contamination rate* by false detections. In the case of LSST, for example, we detect clusters via the observation of their member galaxies in the six LSST bands; X–ray satellites and SZ observations, on the other hand, detect clusters through their hot intracluster medium. In the following, we refer to the completeness function as $\Pi\left(M, z, \Theta_N\right)$ and treat it as a function of halo mass M, redshift z and a set of parameters Θ_N. The latter depend

[4] http://sci.esa.int/science-e/www/area/index.cfm?fareaid=17
[5] http://www.mpe.mpg.de/projects.html#erosita

on the nature of the cluster detection algorithm and describe both observational effects as well as astrophysical effects tied to cluster physics.

In addition to position and redshift, we characterize our clusters with a set of measurable observables, $\vec{O}$, such as member galaxy count (richness), X-ray flux or SZ signal. Via the cluster scaling relations, we use these to construct an estimate of cluster mass, referred to in the following as the cluster *observable mass*, M_O. The key quantity then is the distribution between the observable mass and true cluster halo mass, M: $P\left(M_O|M,z,\Theta_N\right)$. Specifically, this is the probability distribution of M_O given the true mass M and redshift; it also depends on a number of parameters, most notably astrophysical parameters describing cluster physics, which we include among the nuisance parameters, Θ_N.

The objective is to relate the observed cluster distribution to the theory through the cosmological parameters, Θ_C:

$$\begin{aligned}\frac{dN}{dzdM_O} &= \frac{dV}{dz}\left(z,\Theta_C\right)\int d\ln M\; P\left(M_O|M,z,\Theta_N\right)\Pi\left(M,z,\Theta_N\right)\frac{dn}{d\ln M}\left(M,z,\Theta_C\right) \\ &\quad + \left.\frac{dN}{dzdM_O}\right|_{false}\end{aligned} \tag{13.15}$$

Here, the last term accounts for catalog contamination and the quantity $dn/d\ln M$ is the mass function of dark matter halos giving their co-moving number density as a function of mass, redshift and cosmological parameters. This function can be written as

$$\frac{dn}{d\ln M} = \frac{\bar{\rho}}{M}F(M,z,\Theta_C) \tag{13.16}$$

where $\bar{\rho}$ as the co-moving mass density and the function, F, as the multiplicity function – often simply referred to as the mass function itself. Numerical N–body simulations confirm the theoretical expectation (Jenkins et al. 2001) for a universal function, F, dependent only on the amplitude of the matter power spectrum at each redshift: $\sigma(M,z,\Theta_C) = g(z,\Theta_C)\sigma(M,z=0,\Theta_C)$, where g is the linear growth factor (defined so that $g = 1$ at $z = 0$). In Gaussian theories, the mass function is, in fact, an exponential function of this amplitude, giving the method strong leverage on cosmological parameters.

The cosmological parameters are constrained by fitting the above equation to the observed distribution, $dN/dzdM_O$, and marginalizing over the nuisance parameters, Θ_N, incorporating as much prior information as possible on the latter. The nuisance parameters account for a host of systematic effects in the procedure, and their proper definition is crucial to an unbiased cosmological analysis including the selection effects of the sample. Properly defined nuisance parameters allow us to incorporate what are often strong prior constraints on their values when marginalizing in the final analysis.

Mock catalogs of a given survey and catalog construction algorithm guide the choice of parameters describing the selection function. We also empirically control cluster selection functions by comparing different kinds of surveys, e.g., optical versus X-ray versus SZ surveys, all of which will be available in the LSST era. The LSST survey will, in fact, find so many clusters that we will be able to use comparison of different catalog construction methods and different selection cuts on the survey data itself as a powerful control of the selection function.

Parameters of the observable mass-distribution are primarily related to cluster physics, a subject of great interest in its own right. Cluster masses can be determined directly through application of the virial theorem to member galaxy dynamics, through application of hydrostatic equilibrium to observations (X–ray, SZ) of the intracluster medium, and through gravitational lensing experiments. The latter two methods have been particularly powerful in the establishment of cluster scaling relations in recent years. With LSST we will use gravitational lensing to constrain the observable–mass relation; for example, by stacking objects it is possible to calibrate the mean relation down to very low masses (e.g., Johnston et al. 2007b). Furthermore, LSST lensing measurements will help calibrate observable mass relations for other wavebands, such as the X–ray and millimeter (SZ catalogs).

13.6.2 The LSST Cluster Catalog

Numerous methods exist and have successfully been used for finding clusters in large multi-band imaging surveys. They are distinguished by their emphasis on different aspects of the cluster galaxy population. This is a strength, because it will be important to implement a variety of cluster detection methods to best understand the selection criteria defining the final catalog. All methods provide, in the end, a list of cluster positions, photometric redshifts, and observable properties, such as richness, total luminosity, and so on. We here describe one such method, based on Voronoi tessellation of galaxies on the red sequence. Many other approaches, including matched filters, will also be considered.

The Cluster Red Galaxy Population

Most detection methods rely on the presence of the characteristic red, early-type galaxy population in clusters, which displays a well–defined color-magnitude relation known as the "red sequence" (RS). The detectability of this population as a function of cluster mass and redshift is therefore a central issue for most detection algorithms.

To address this point, we show the estimated mass detection threshold as a function of redshift, $M_{det}(z)$, individually for the LSST r, i, z and y bands in Figure 13.11. We consider as detected those clusters for which ten red–sequence galaxies with $L_R > 0.4L*$ are seen at $> 10\sigma$ in the band in question. For our cluster model we use red–galaxy conditional luminosity functions from SDSS (Yang et al. 2008) evolved with passive stellar evolution to higher redshift (Fromenteau et al., in preparation). Fromenteau et al. examine the appropriateness of passive evolution by comparing the cluster red galaxy luminosity functions from this model to luminosity functions extracted from the halo occupation distribution (§ 9.4) constrained in the NOAO deep wide field by Brown et al. (2008).

That comparison supports the idea that the colors of red sequence cluster populations are well described by passive evolution out to $z \sim 1$. Less certain is what fraction of clusters will *possess* a red sequence, however, and how many members that red sequence will have. A number of studies have found that the abundance of red galaxies with luminosities of $L*$ and below has increased by a factor of 2-4 since $z \sim 1$ (Brown et al. 2008; Willmer et al. 2006), so we know the overall red sequence population must have grown since $z \sim 1$. Detailed investigations of galaxy populations

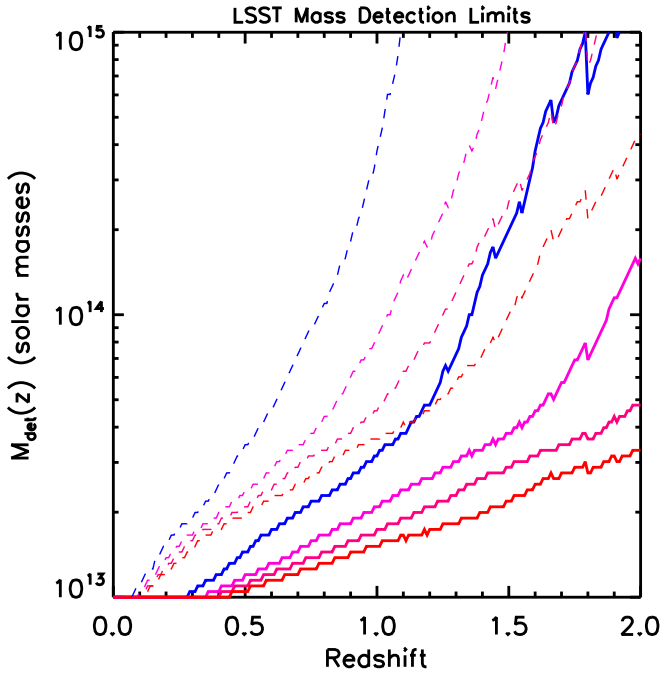

Figure 13.11: Minimum detectable cluster mass as a function of redshift for r, i, z and y bands (blue to red curves). Cluster detection requires at least ten red–sequence galaxies detected in–band at $10\,\sigma$ and with $L_R > 0.4L_*$ (Fromenteau et al., in preparation). The dashed lines correspond to single-visit images and the solid lines to the complete ten–year survey.

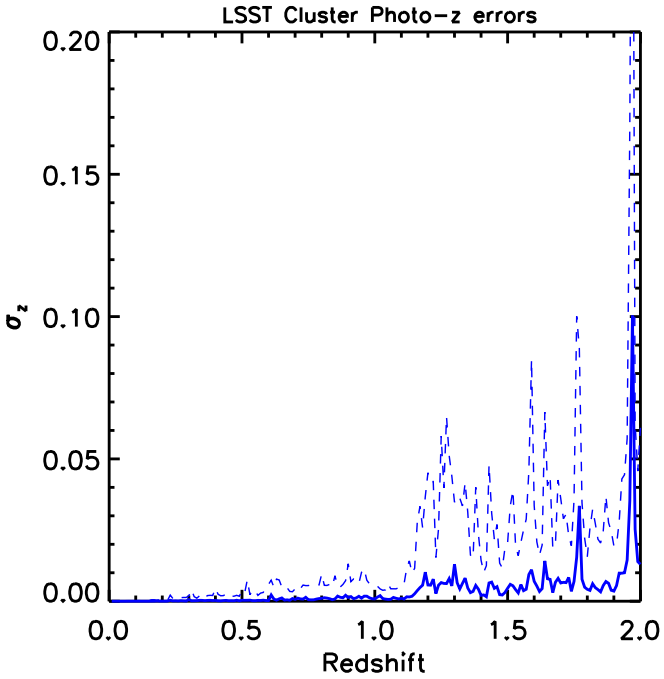

Figure 13.12: Estimated cluster photometric redshift errors for single–visit (dashed) and full ten-year (solid) survey images. They are underestimated because the model uses a single red–galaxy template, but give an idea of the expected errors and their variation with redshift.

in groups and low-mass clusters (Gerke et al. 2007) and of the dependence of galaxy color on environment (Cooper et al. 2007) to $z \sim 1.4$ have found that the fraction of red galaxies in clusters of modest mass ($\gtrsim 10^{13}\,M_\odot$) is indistinguishable from the fraction in the field at $z \sim 1.35$, but grows steadily at lower redshifts. Since it takes ~ 1 Gyr for a galaxy's color to turn red after star formation ends, this requires that star formation began to be strangled in clusters with a mass of $\gtrsim 10^{13}\,M_\odot$ around redshift 2, with the process ongoing to $z = 1$ or beyond. However, at least some massive systems *do* contain a well-defined red sequence at $z > 1$; e.g., the $z = 1.24$ system studied by Figure 9.8.

As expected in hierarchical structure formation models, it appears that galaxy evolution proceeds fastest in the most massive clusters, which also will host the most massive galaxies. In those systems, a red sequence may be apparent by $z \sim 1.5 - 2$, while in lower-mass clusters or groups it may appear only after $z \sim 1$. This is predicted in models where the near total quenching of star formation necessary to produce a red sequence galaxy requires the presence of a dark matter halo above the threshold mass where cooling becomes inefficient (e.g., Silk 1977; Rees & Ostriker 1977; Binney 1977; White & Rees 1978; Croton et al. 2006). In such a scenario, massive clusters pass that threshold mass at $z \sim 3$, while a typical weak cluster or group will pass it at $z \sim 2$ or later, consistent with observations. Our uncertainty in the evolution of galaxies within clusters to high redshift is one reason it will be important to compare cluster samples selected via different means.

Assuming the the red sequence galaxy fraction does not change with redshift, LSST will be able to detect clusters well down into the group range, in both single visit and complete survey images (Figure 13.11). The mass threshold decreases as we move redward because the RS galaxies are dominated by red light, and inflects upwards in a given band when the 4000Å break moves through that band. Single visit r, i and z images will be comparable in depth to the Dark Energy Survey (DES) survey. The LSST y band and the deeper imaging of the complete survey will allow us to go to appreciably higher redshifts at a given mass threshold than is possible for DES.

In Figure 13.12 we give an estimate of the expected photometric redshift errors for a cluster of $10^{14}\,M_\odot$ as a function of redshift (Fromenteau et al., in preparation). The errors are slightly underestimated, especially at low redshift, because we have only employed a single galaxy template for this estimate. Nevertheless, we see that cluster photometric redshifts should be very good out to redshift unity, after which they suffer some degradation for single visit images; the degradation, however, is not severe. The redshift precision remains very good out to $z = 2$ with the deeper complete survey images.

Galaxy Cluster Finder: Red-Sequence Voronoi Tessellation and Percolation Method

The detection of galaxy clusters based on the red-sequence Voronoi tessellation and percolation method (VTP) utilizes the red-sequence property of early-type cluster galaxies. The method works by dividing the galaxy spatial plane into polyhedral cells, each containing a unique galaxy (see Figure 13.13). The cells are then grouped together using a percolation method, and galaxy clusters are detected as over densities of cells from that expected for a random distribution. In order to maximize the signal-to-noise ratio of a given cluster above the background field population, the galaxy plane is first divided into multiple overlapping red-sequence slices based on the expected color of early-type cluster galaxies for a range in redshifts (Figure 13.14). Galaxy clusters are then

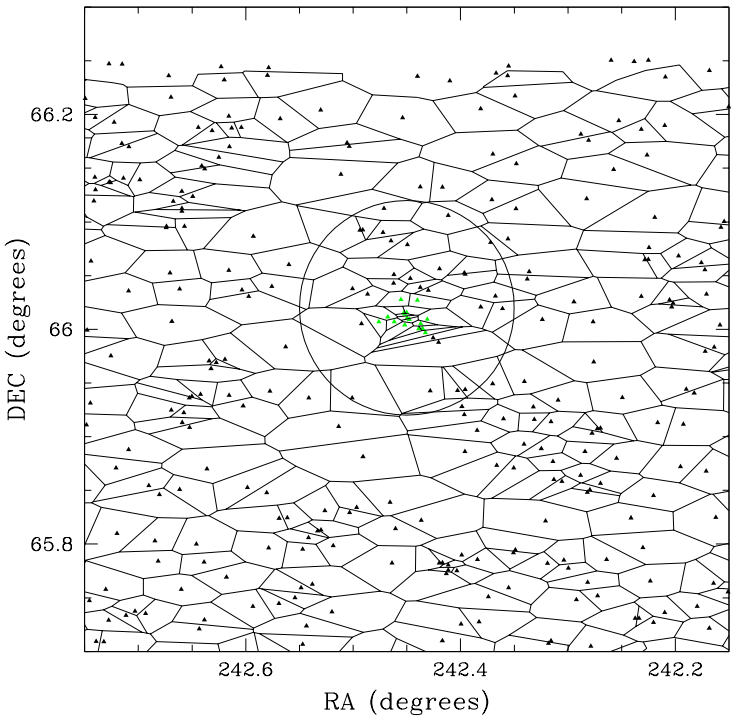

Figure 13.13: The Voronoi tessellation on the galaxy distribution (from the CTIO and KPNO 4-m telescopes) in the field of an extended X-ray source observed by Chandra. Only galaxies satisfying the $r - i$ color cut expected for a cluster red sequence at $z = 0.475$ are depicted. The imaging data used here do not go as deep as a single LSST visit. Figure from Barkhouse et al. (2006), with permission.

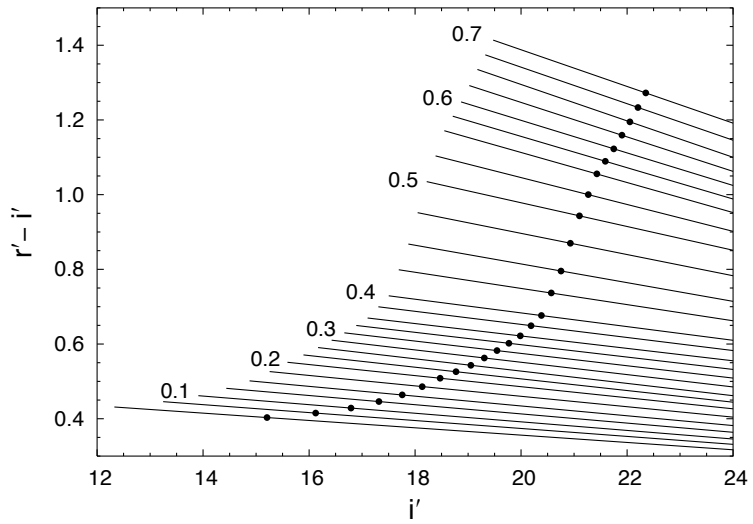

Figure 13.14: Selected red-sequence model color slices used to choose galaxies for a range of redshifts (indicated to the left of the lines) for the VTP cluster detection method (Barkhouse et al. 2006). The solid circles indicate positions of the brightest cluster galaxies. Figure from Barkhouse et al. (2006), with permission.

detected using individual color slices, with overlapping detections in adjacent slices merged based on the significance of the detected clusters as output by the VTP algorithm. The non-parametric VTP method employs no assumption regarding cluster shape; thus the VTP technique is sensitive to symmetric as well as irregular clusters. However, with this and other optical cluster-finding algorithms, it will be necessary to determine the relationship of the identified systems to the individual virialized halos counted in cosmological tests; e.g., these techniques will often identify the combined population of groups along the line of sight as belonging to a single cluster (e.g., Gladders et al. 2007).

Relation to Other Cluster Catalogs (X–ray, SZ, IR, Shear)

SZ Cluster Scaling Relations

Sealfon et al. (2006) showed how to place constraints on cluster physics by stacking the weak lensing signal from multiple clusters found through the SZ effect. The next generation of SZ surveys will provide a catalog of thousands of clusters (Carlstrom et al. 2002). The SZ flux is proportional to the integral of the product of the density and the temperature of the hot gas in the cluster (Sunyaev & Zeldovich 1980), and the flux limit of the catalogs will approximately translate into a mass limit. However, the actual value of the cluster's mass for a given SZ flux depends on the details of the SZ-mass relation, which in turn is governed by cluster physics. Cluster scaling relations involving SZ have been extensively studied as a tool to investigate cluster physics (e.g., da Silva et al. 2004; Benson et al. 2002; McCarthy et al. 2003; Verde et al. 2002).

Recent work has explored the SZ-mass relation using numerical simulations (e.g., Oh & Benson 2003; da Silva et al. 2004; Motl et al. 2005; Nagai 2005) and analytical approximations (e.g., Dos Santos & Doré 2001; Reid & Spergel 2006; Roychowdhury et al. 2005; Ostriker et al. 2005). Numerical models find that the SZ-mass relation is expected to be very tight, implying that cluster masses can be directly read out from the SZ observations once the SZ-mass relation has been calibrated.

One possibility is to calibrate this relation on cosmological simulations, but this requires understanding and modeling all the relevant baryonic physics. Alternatively, we would like a robust method to estimate cluster masses directly from observations, independently of intra-cluster medium (ICM) modeling, and without relying on numerical simulations. Gravitational lensing provides the most direct way to measure the mass of clusters, and we discuss this in detail in § 12.12 and § 14.3.8.

With ground-based experiments, a direct mass determination is possible only for fairly massive clusters, $\approx 10^{15}\,M_{\odot}$ (e.g., Marian & Bernstein 2006). However Sealfon et al. (2006) argue that by stacking the weak lensing signals from multiple clusters with roughly the same SZ luminosity, otherwise undetectable shear signal can be amplified, allowing one to determine an average mass in bins of SZ luminosity.

While a non-parametric technique to reconstruct the average mass profile from measurements of clusters-shear correlation function has been presented in Johnston et al. (2007a,b), for this signal-to-noise ratio calculation we will take a complementary approach followed by Sealfon et al. (2006):

$\Delta z = 0.2$	M-$L_{\rm SZ}$		M-y_0	
bin	Amplitude	Slope	Amplitude	Slope
$z \sim 0.1$	2.8%	2.4%	2.4%	3.6%
$z \sim 0.5$	1.6 %	1.2%	1.6%	2.4%
$z \sim 1$	9 %	9%	5.3%	12%

Table 13.1: Forecasted fractional errors on the slope and amplitude of the scaling relations between mass and SZ luminosity and Compton parameter y_0. Despite having larger scatter, the M-y_0 relation is flatter, yielding fractional errors on the amplitude comparable (or better) than those for the M-$L_{\rm SZ}$ relation.

we assume a cluster profile (a Navarro-Frenk-White (NFW) radial cluster profile; Navarro et al. 1997) and we will recover the average mass.

Both the total SZ luminosity and the central Compton parameter y_0 are expected to depend on cluster mass approximately as power laws, with some intrinsic scatter. It is customary to parametrize these relations over a range of masses as power laws with two free parameters (an amplitude and a slope of a linear fit in log-log space) and study how these parameters are expected to change for different assumptions about cluster physics.

Table 13.1 shows the constraints on these parameters from a 5000 deg^2 SZ survey overlapping the LSST footprint. Given these errors, we will be able to distinguish at more than the $3\,\sigma$ level between:

- A self-similar model with only gravitational physics (i.e. no heating nor cooling), where the gas temperature is given solely by the dark matter virial temperature;
- a model with a pre-heating and a cooled gas fraction of $f_{cool} = 0.42$;
- a model with an accretion pressure decreased by a factor of 3.5 from self-similar spherical collapse;
- a model with an accretion pressure increased by a factor of 3.5 from self-similar spherical collapse;
- a purely adiabatic cluster model from one that includes cooling and a star formation model;
- models in which the exponent of the radial entropy profile are 1.1 and 1.5, respectively; and
- models in which the entropy profile normalization differ by a factor of 1.5.

These small error bars suggest that we may be able to constrain how the mass-SZ scaling evolves with redshift. A mass measurement from weak lensing and a SZ measurement in different redshift bins can constrain the evolution of hot gas as a function of redshift, which in turn would enable one to constrain feedback evolution.

The approach presented here can, of course, be applied also to other analytical models and to predictions from numerical work. In the cases where the two-parameter fit yields a S/N > 5, one could add parameters to the fit to test, e.g., if deviations from a power law in the scaling relation can yield additional information about cluster physics.

13.7 Cross-Correlations with the Cosmic Microwave Background

Ryan Scranton, Leopoldo Infante

Cross-correlations between a large galaxy survey like the LSST and a map of the cosmic microwave background radiation from either WMAP or Planck can provide a number of useful measurements of various physical processes. The most studied of these is the detection of the late Integrated Sachs-Wolfe (ISW) effect (Sachs & Wolfe 1967), a positive cross-correlation between foreground galaxies and background CMB temperature induced by dark energy. In the first year of operation, LSST should measure the ISW effect to greater precision than current efforts involving combinations of galaxy catalogs from multiple sources. Over the longer term, measuring the ISW with LSST has the potential to provide unique insight into the nature of dark energy by placing constraints on the smoothness of the dark energy potential at the 3-5% level on scales around 1 Gpc. The richness of the LSST galaxy sample will also allow us to greatly expand upon related measurements involving galaxy-CMB cross-correlations. This will include magnification-induced ISW signal at high redshifts, ISW detection using superclusters and voids and cluster peculiar velocity measurements through the kinetic Sunyaev-Zel'dovich effect.

13.7.1 Dark Energy and Structure Formation

As the Universe expands, light travels from the surface of last scattering through the intervening large scale structure to observers here on Earth. In doing so, it passes through any number of local gravitational potentials (i.e., regions in which structure is forming), experiencing a gravitational blueshift as they fall into the potential and a redshift as they exit it. During the matter-dominated phase of the Universe's evolution (when $\Omega_{matter} \approx 1$), the rate of structure growth matches the rate of universal expansion to first order, so the extra energy lost by photons climbing out of potential wells that have been growing during the photon's traversal matches the general expansion of the Universe. Thus, the photon energy is practically identical to one that avoided the potential altogether. As the Universe transitions to a dark energy dominated phase, the universal expansion begins to accelerate, outpacing the growth of structure. Hence, photons passing through intervening potentials will not lose all the energy they gained when they entered, as the potential wells are shallower as they leave. This induces a positive correlation between the background CMB temperature and the projected matter (or galaxy) density.

The first measurements of the ISW effect were done using CMB maps from the COBE DMR mission cross-correlated with the NVSS (radio) and HEAO-1 (X-ray) galaxy surveys. With the release of higher resolution CMB maps from WMAP, a second wave of analysis was done cross-correlating the CMB against galaxy surveys from 2MASS (Afshordi et al. 2004), SDSS (Scranton et al. 2003; Fosalba et al. 2003), NVSS (Raccanelli et al. 2008), and the photometric quasar survey from the SDSS (Giannantonio et al. 2006). Each of these measurements yielded detections of the expected signal in the 2-3 σ range. The current state of the art comes from combining the various measurements from the various surveys into a single detection (Giannantonio et al. 2008; Ho et al. 2008). This allows for a redshift coverage from $0 < z < 2$, albeit with varying sky coverage over the course of that range. These assemblies yield detections in the 3.5-4.5 σ range. While the ISW signal itself is not currently capable of constraining cosmological parameters to the extent of other

probes, its likelihood contours are very complementary to those from baryon acoustic oscillations, CMB, supernovae, and weak lensing.

13.7.2 ISW Formalism

The ISW effect dominates the cross-correlation signal at an angular scale of $\theta \gtrsim 1^\circ$ (at this scale, the choice of WMAP or Planck for the CMB map should be irrelevant), while at smaller angular scales, the signal is dominated by the thermal SZ effect. The cross-correlation function of fields A and B, $\omega_{AB}(\theta)$ can be written in terms of the angular power spectrum multipoles ($C_{AB}(l)$) by expanding it with Legendre polynomials,

$$\omega_{AB}(\theta) \;=\; \sum_{l=0}^{\infty} \frac{(2l+1)}{4\pi} C_{AB}(l) P_l(\cos\theta), \tag{13.17}$$

where P_l is the Legendre polynomial of order l. It is possible to show that for small angles, or large l, (Afshordi et al. 2004; Cooray 2002)

$$C_{AB}(l) \;=\; \int_0^\infty \frac{dr}{r^2}\; P(k)\; W^A(k,r)\; W^B(k,r), \tag{13.18}$$

where $P(k)$ is the initial power spectrum of matter, $k = \frac{l+1/2}{r}$, and $W^X(k,r)$ is the window function of the field X. This approximation holds up to a good degree of accuracy for $l \geq 2$.

The window function of the anisotropy field in the CMB map generated by the ISW effect can be written as

$$W^{ISW}(r,k) \;=\; -3T_0\; \frac{\Omega_m}{k^2} \frac{H_0^2}{c^2} \frac{\partial G(z)(1+z)}{\partial z}, \tag{13.19}$$

where T_0 is the mean temperature of the CMB, Ω_m is the matter density of the Universe in units of the critical density, H_0 is Hubble's constant, c is the speed of light, and $G(z)$ is the growth factor of the gravitational potential.

For the galaxy side, the window function is given by

$$W^g \;=\; b_g\; \frac{H(z)}{c}\; G(z)\; n(z), \tag{13.20}$$

where b_g is the bias factor, $H(z)$ is the Hubble parameter as a function of redshift, and $n(z)$ is the galaxy density distribution, which will depend directly on the characteristics of the observations. This model of bias is very simple, obviously, but we are only interested in the signal on large scale and, as will be seen shortly, the signal-to-noise ratio is independent of our choice.

The variance ($\sigma^2_{C_{gT}}$) on each multipole of the angular cross-power spectrum, (C_{gT}), is given by

$$\sigma^2_{c_{gT}}(l) \;=\; \frac{1}{f_{sky}(2l+1)} \left\{ C^2_{gT}(l) + C_{TT}(l) \left[C_{gg}(l) + \frac{1}{\bar{N}} \right] \right\}, \tag{13.21}$$

where C_{TT} and C_{gg} are the CMB and galaxy angular power spectra, respectively. $\bar{N}$ is the mean number of galaxies per steradian on the survey (the "shot-noise" term in the galaxy map) and

f_{sky} is the fraction of the sky used for the cross-correlation. This can be propagated to the cross-correlation function, such that

$$\sigma^2_{\omega_{gT}} = \sum_l \frac{(2l+1)}{f_{sky}(4\pi)^2} P_l^2(\cos\theta) \left\{ C^2_{gT}(l) + C_{TT}(l) \left[C_{gg}(l) + \frac{1}{\bar{N}} \right] \right\}. \quad (13.22)$$

13.7.3 Cross-Correlating the CMB and the Stacked LSST Galaxy Sample

With the full LSST survey, we will be able to cross-correlate the CMB fluctuations with different subsamples of galaxies selected by redshift or type. This will allow us to measure how the ISW signal changes over the course of the history of the Universe, how different populations experience multiple effects that contribute to their cross-correlation with the CMB, and how the local over-(under-)densities contribute to the correlation.

Dark Energy Clustering

As mentioned above, the ISW constraints on the cosmological parameters for the fiducial model (Appendix A) are relatively weak. However, for more exotic models of dark energy this is not true. In particular, if the dark energy field can cluster, ISW measurements become our best means to detect this effect, which would be a key indicator for physical dark energy models.

Hu & Scranton (2004) consider a dark energy model where the clustering is parametrized by the sound speed (c_s) of the dark energy field (which we here assume to be independent of w). Given this speed, one can determine a scale η at which perturbations in the fluid enter the horizon and begin to gravitationally collapse. At this point, dark energy would begin to fall into gravitational potentials on the largest scales, and the freezing out process that began as dark energy became the driver for the expansion of the Universe would reverse itself. Since this happens on the largest scales and proceeds inward, the effect would be first detectable in the ISW effect, as well as presenting the longest baseline for measuring dark energy clustering.

For the calculations presented in Hu & Scranton (2004), the fiducial model used has $w = -0.8, c_S = 0.1\,c$. The survey depth considered is 70 galaxies arcmin^{-2}, which is approximately what would be possible with LSST if we only require $10\,\sigma$ photometry in the three deepest bands (§ 3.7.2). With these model parameters, they estimate that the smoothness of the dark energy potential could be constrained at 3% on scales of 1 Gpc. While c_s remains largely unconstrained by current measurements, the combined constraints from CMB, baryon oscillations, and supernovae put the value of w used in those calculations outside of the 95% contours for a constant w model.

Magnification

The peak in expected ISW S/N for a ΛCDM cosmology happens for galaxies around $z \sim 0.5$. The window function for the CMB side of the cross-correlation peaks at $z = 0$, but the competing volume effects push the peak in S/N to somewhat higher redshift. For $z > 1$, the effects of a cosmological constant are generally too small to generate a deviation from simple CDM growth

measurable via the ISW effect. However, as pointed out by Loverde et al. (2007), this ignores the effects of magnification.

For higher redshift samples, we need to include the effect of lensing by foreground structure. While the dark matter potentials will not have experienced significant decay at those redshifts, the galaxies inside those potentials will be lensed by foreground structures where the ISW effect is considerably stronger. This replaces the galaxy window function from Equation 13.20 with

$$W^{\mu,i} = 3\Omega_m \frac{H_0^2}{c^2}(2.5s_i - 1)\ G(z)\ (1+z)g(z, z_i), \tag{13.23}$$

where s_i is the power-law slope of a given photometric redshift bin's galaxy number counts. $g(z, z_i)$ is the lensing weight function for that redshift bin,

$$g(z, z_i) = \chi(z) \int dz' \frac{\chi(z') - \chi(z)}{\chi(z')} n_i(z'), \tag{13.24}$$

where χ is the comoving distance and $n_i(z)$ is the redshift distribution for the bin. For a given set of galaxies around χ, g will peak at roughly $\chi/2$. This, in turn, implies that even a set of galaxies at $z > 2$ can experience significant cross-correlation with the CMB due to lensing by galaxies at much lower redshift. This signal is, of course, dependent on the value of s for that sample, although as pointed out by Ménard & Bartelmann (2002), one can apply an optimal estimator where each galaxy is weighted by $2.5s - 1$, which only yields a null result for $s = 0.4$.

Using two samples which are roughly equivalent to the first year and full LSST data set, Loverde et al. (2007) show that the contribution of magnification for a given high redshift bin ($z \sim 3.5$) can result in nearly an order of magnitude increase in the expected cross-correlation. This in turn leads to an increase in the S/N at those redshifts, although the aggregate S/N as a function of redshift does not improve significantly due to strong correlations between the signals in each redshift bins induced by the magnification. More importantly, including the effects of magnification improves the constraints on w at higher redshift from ISW by roughly a factor of 2, bringing them in line with the constraints at lower redshifts ($\delta w \sim 0.2$ at $z \sim 1$). With the galaxy color information available in LSST, this could be further enhanced by looking at galaxy sub-populations like luminous red galaxies or Lyman-break galaxies which have especially steep number count relations ($2.5s - 1 \gtrsim 2$).

Superclusters and Voids

The standard detection of the ISW effect is through cross-correlation between the local large scale structure and CMB temperature fluctuations. These detections have been at levels below 3σ. In coming years through large area surveys (DES, VST, and so on), the S/N for ISW detection will be increased by perhaps $\sim 50\%$ and by a factor of 4 with the early LSST 20,000 deg^2 data. A recent paper by Granett et al. (2008) claims a $S/N > 4$ detection of the ISW effect. To trace the highest and lowest density peaks, which presumably trace the highest and lowest mass structures, they identified 50 candidate superclusters and 50 potential supervoids at redshifts ~ 0.5 from the SDSS data. They stacked the WMAP five-year temperature pixels corresponding to these regions, and found an increase in temperature towards the potential superclusters and a decrease towards the potential supervoids, detecting the ISW effect at above 4 σ.

To carry out this experiment with LSST, we will need to clearly identify massive supercluster-scale structures on scales up to 150 Mpc. LSST will provide photometric redshifts as good as $0.02(1+z)$ for luminous red galaxies (LRGs) (§ 3.8). We will be able to identify coherent structures to $z \sim 1.5$, where $\Delta z \sim 0.04$ corresponds to $\Delta(D_{com}) \sim 93$ Mpc or $\theta \sim 3°$.

Extrapolating from the Granett et al. (2008) results and scaling by the larger solid angle of the LSST analysis, we estimate that we will be able to detect the ISW effect in this way to $7\,\sigma$ total using perhaps half a dozen redshift shells to $z \sim 2$.

13.8 Education and Public Outreach

Eric Gawiser, Suzanne H. Jacoby

The Large-Scale Structure Science Collaboration explores "the big picture" of how the Universe is organized on a grand scale and over grand expanses of time. Characterizing the evolution of the distribution of matter on extragalactic scales is a primary science goal. The large-scale structure of the Universe encodes crucial information about its contents, how it is organized and how this organization has evolved with time. This way of viewing the Universe is well aligned with several "big ideas" in science education reform as described in Project 2061: Science for All Americans[6] and the National Science Education Standards (National Research Council 1996). These ideas, called Unifying Concepts, include concepts such as systems, order, and organization; patterns of change, evolution, and scale. Unifying Concepts can serve as a focus for instruction at any grade level; they provide a framework within which science can be learned and a context for fostering an understanding of the nature of science. The Large-Scale Structure team will support the EPO group in providing this framework of Unifying Concepts in materials developed for classroom learning experiences.

One thread of the LSST Education and Public Outreach program emphasizes visualization of LSST data in science centers and on computer screens of all sizes. Each LSST public data release can be viewed using two- and three-dimensional visualization programs (e.g., Google Sky, WWT, the Digital Universe). Large-Scale Structure Science Collaboration team members will assist informal science centers in incorporating the LSST data into their visualization platforms and conveying their meaning to the public. This will enable LSST discoveries to be featured in weekly, live planetarium shows and to actively involve our audience in LSST's mission of mapping the structure of all matter in the Universe. The use of LSST data in an informal museum or science center setting represents an ideal opportunity to expose large numbers of people to the magnificence of the vast LSST data set. Image browsers such as Google Sky, WWT, and the Digital Universe will broaden LSST's availability to everyone with a home computer or laptop (or PDA or cellphone, given the rapid growth of technology), to truly enable visualization on "computer screens of all sizes."

References

Afshordi, N., Loh, Y.-S., & Strauss, M. A., 2004, *Phys. Rev. D*, 69, 083524

[6] http://www.project2061.org/publications/sfaa/default.htm

Albrecht, A. et al., 2009, ArXiv e-prints, 0901.0721
—, 2006, Astrophysics e-prints, arXiv:astro-ph/0609591
Babbedge, T. S. R., Whitaker, R., & Morris, S., 2005, *MNRAS*, 361, 437
Barkhouse, W. A. et al., 2006, *ApJ*, 645, 955
Benson, A. J., Reichardt, C., & Kamionkowski, M., 2002, *MNRAS*, 331, 71
Bernstein, G., 2006, *ApJ*, 637, 598
Bernstein, G., & Huterer, D., 2009, ArXiv e-prints, 0902.2782
Binney, J., 1977, *ApJ*, 215, 483
Blake, C., & Bridle, S., 2005, *MNRAS*, 363, 1329
Blake, C., Collister, A., Bridle, S., & Lahav, O., 2006, ArXiv Astrophysics e-prints, arXiv:astro-ph/0605303
Blake, C., & Glazebrook, K., 2003, *ApJ*, 594, 665
Blanton, M. R., Eisenstein, D., Hogg, D. W., & Zehavi, I., 2006, *ApJ*, 645, 977
Bond, J. R., & Efstathiou, G., 1984, *ApJL*, 285, L45
Bond, J. R., Jaffe, A. H., & Knox, L., 1998, *Phys. Rev. D*, 57, 2117
Brown, M. J. I. et al., 2008, *ApJ*, 682, 937
Carbone, C., Verde, L., & Matarrese, S., 2008, *ApJL*, 684, L1
Carlstrom, J. E., Holder, G. P., & Reese, E. D., 2002, *ARAA*, 40, 643
Cole, S. et al., 2005, *MNRAS*, 362, 505
Cooper, M. C. et al., 2007, *MNRAS*, 376, 1445
Cooray, A., 2002, *Phys. Rev. D*, 65, 103510
Cooray, A., Hu, W., Huterer, D., & Joffre, M., 2001, *ApJL*, 557, L7
Cresswell, J. G., & Percival, W. J., 2009, *MNRAS*, 392, 682
Crocce, M., & Scoccimarro, R., 2008, *Phys. Rev. D*, 77, 023533
Croton, D. J. et al., 2006, *MNRAS*, 365, 11
da Costa, L. N., Vogeley, M. S., Geller, M. J., Huchra, J. P., & Park, C., 1994, *ApJL*, 437, L1
da Silva, A. C., Kay, S. T., Liddle, A. R., & Thomas, P. A., 2004, *MNRAS*, 348, 1401
Dalal, N., Doré, O., Huterer, D., & Shirokov, A., 2008, *Phys. Rev. D*, 77, 123514
Dos Santos, S., & Doré, O., 2001, Astrophysics e-prints, arXiv:astro-ph/0106456
Eisenstein, D. J., & Hu, W., 1999, *ApJ*, 511, 5
Eisenstein, D. J., Hu, W., & Tegmark, M., 1998, *ApJL*, 504, L57
Eisenstein, D. J. et al., 2005, *ApJ*, 633, 560
Fisher, K. B., Davis, M., Strauss, M. A., Yahil, A., & Huchra, J. P., 1993, *ApJ*, 402, 42
Fosalba, P., Gaztañaga, E., & Castander, F. J., 2003, *ApJL*, 597, L89
Fry, J. N., 1994, *Phys. Rev. Lett.*, 73, 215
Gerke, B. F. et al., 2007, *MNRAS*, 376, 1425
Giannantonio, T. et al., 2006, *Phys. Rev. D*, 74, 063520
Giannantonio, T., Scranton, R., Crittenden, R. G., Nichol, R. C., Boughn, S. P., Myers, A. D., & Richards, G. T., 2008, *Phys. Rev. D*, 77, 123520
Gladders, M. D., Yee, H. K. C., Majumdar, S., Barrientos, L. F., Hoekstra, H., Hall, P. B., & Infante, L., 2007, *ApJ*, 655, 128
Granett, B. R., Neyrinck, M. C., & Szapudi, I., 2008, ArXiv e-prints, 0805.2974
Ho, S., Hirata, C., Padmanabhan, N., Seljak, U., & Bahcall, N., 2008, *Phys. Rev. D*, 78, 043519
Hoekstra, H., van Waerbeke, L., Gladders, M. D., Mellier, Y., & Yee, H. K. C., 2002, *ApJ*, 577, 604
Holtzman, J. A., 1989, *ApJS*, 71, 1
Hu, W., & Haiman, Z., 2003, *Phys. Rev. D*, 68, 063004
Hu, W., & Jain, B., 2004, *Phys. Rev. D*, 70, 043009
Hu, W., & Okamoto, T., 2004, *Phys. Rev. D*, 69, 043004
Hu, W., & Scranton, R., 2004, *Phys. Rev. D*, 70, 123002
Huff, E., Schulz, A. E., White, M., Schlegel, D. J., & Warren, M. S., 2007, *Astroparticle Physics*, 26, 351
Jenkins, A., Frenk, C. S., White, S. D. M., Colberg, J. M., Cole, S., Evrard, A. E., Couchman, H. M. P., & Yoshida, N., 2001, *MNRAS*, 321, 372
Johnston, D. E., Sheldon, E. S., Tasitsiomi, A., Frieman, J. A., Wechsler, R. H., & McKay, T. A., 2007a, *ApJ*, 656, 27
Johnston, D. E. et al., 2007b, ArXiv e-prints, 0709.1159
Kaiser, N., 1984, *ApJL*, 284, L9
—, 1992, *ApJ*, 388, 272

Knox, L., Song, Y.-S., & Zhan, H., 2006, *ApJ*, 652, 857
Komatsu, E. et al., 2009, *ApJS*, 180, 330
Lahav, O. et al., 2002, *MNRAS*, 333, 961
Liddle, A. R., & Lyth, D. H., 2000, Cosmological Inflation and Large-Scale Structure, A. R. Liddle & D. H. Lyth, eds.
Limber, D. N., 1954, *ApJ*, 119, 655
Lin, H., Kirshner, R. P., Shectman, S. A., Landy, S. D., Oemler, A., Tucker, D. L., & Schechter, P. L., 1996, *ApJ*, 471, 617
Linder, E. V., 2003, *Phys. Rev. D*, 68, 083504
Liske, J., Lemon, D. J., Driver, S. P., Cross, N. J. G., & Couch, W. J., 2003, *MNRAS*, 344, 307
Loverde, M., & Afshordi, N., 2008, *Phys. Rev. D*, 78, 123506
Loverde, M., Hui, L., & Gaztañaga, E., 2007, *Phys. Rev. D*, 75, 043519
—, 2008, *Phys. Rev. D*, 77, 023512
Ma, Z., Hu, W., & Huterer, D., 2006, *ApJ*, 636, 21
Marian, L., & Bernstein, G. M., 2006, *Phys. Rev. D*, 73, 123525
Matarrese, S., & Verde, L., 2008, *ApJL*, 677, L77
McCarthy, I. G., Babul, A., Holder, G. P., & Balogh, M. L., 2003, *ApJ*, 591, 515
Ménard, B., & Bartelmann, M., 2002, *A&A*, 386, 784
Metcalfe, N., Shanks, T., Campos, A., McCracken, H. J., & Fong, R., 2001, *MNRAS*, 323, 795
Miller, C. J., & Batuski, D. J., 2001, *ApJ*, 551, 635
Miller, C. J., Nichol, R. C., & Chen, X., 2002, *ApJ*, 579, 483
Mo, H. J., Jing, Y. P., & White, S. D. M., 1997, *MNRAS*, 284, 189
Motl, P. M., Hallman, E. J., Burns, J. O., & Norman, M. L., 2005, *ApJ*, 623, L63
Nagai, D., 2005, Astrophysics eprint, ArXiv:astro-ph/0512208
National Research Council, 1996, National Science Education Standards. National Academy Press, 22.
Navarro, J. F., Frenk, C. S., & White, S. D., 1997, *ApJ*, 490, 493
Newman, J. A., 2008, *ApJ*, 684, 88
Norberg, P. et al., 2001, *MNRAS*, 328, 64
Oh, S. P., & Benson, A. J., 2003, *MNRAS*, 342, 664
Ostriker, J. P., Bode, P., & Babul, A., 2005, *ApJ*, 634, 964
Padmanabhan, N. et al., 2006, ArXiv Astrophysics e-prints, arXiv:astro-ph/0605302
Park, C., Vogeley, M. S., Geller, M. J., & Huchra, J. P., 1994, *ApJ*, 431, 569
Peacock, J. A., & Dodds, S. J., 1996, *MNRAS*, 280, L19
Peebles, P. J. E., & Yu, J. T., 1970, *ApJ*, 162, 815
Peiris, H. V. et al., 2003, *ApJS*, 148, 213
Percival, W. J. et al., 2001, *MNRAS*, 327, 1297
Percival, W. J., Cole, S., Eisenstein, D. J., Nichol, R. C., Peacock, J. A., Pope, A. C., & Szalay, A. S., 2007a, *MNRAS*, 381, 1053
Percival, W. J. et al., 2007b, *ApJ*, 657, 645
—, 2009, ArXiv e-prints, 0907.1660
Pozzetti, L., Madau, P., Zamorani, G., Ferguson, H. C., & Bruzual A., G., 1998, *MNRAS*, 298, 1133
Press, W. H., & Schechter, P., 1974, *ApJ*, 187, 425
Raccanelli, A., Bonaldi, A., Negrello, M., Matarrese, S., Tormen, G., & de Zotti, G., 2008, *MNRAS*, 386, 2161
Rees, M. J., & Ostriker, J. P., 1977, *MNRAS*, 179, 541
Reid, B. A., & Spergel, D. N., 2006, *ApJ*, 651, 643
Retzlaff, J., Borgani, S., Gottlober, S., Klypin, A., & Muller, V., 1998, *New Astronomy*, 3, 631
Roychowdhury, S., Ruszkowski, M., & Nath, B. B., 2005, Astrophysics e-prints, arXiv:astro-ph/0508120
Ruhl, J. et al., 2004, Society of Photo-Optical Instrumentation Engineers (SPIE) Conference Series, Vol. 5498, The South Pole Telescope, C. M. Bradford, P. A. R. Ade, J. E. Aguirre, J. J. Bock, M. Dragovan, L. Duband, L. Earle, J. Glenn, H. Matsuhara, B. J. Naylor, H. T. Nguyen, M. Yun, & J. Zmuidzinas, eds. pp. 11–29
Sachs, R. K., & Wolfe, A. M., 1967, *ApJ*, 147, 73
Scherrer, R. J., & Weinberg, D. H., 1998, *ApJ*, 504, 607
Schlegel, D. J., Finkbeiner, D. P., & Davis, M., 1998, *ApJ*, 500, 525
Schneider, M., Knox, L., Zhan, H., & Connolly, A., 2006, *ApJ*, 651, 14
Scranton, R. et al., 2003, ArXiv Astrophysics e-prints, arXiv:astro-ph/0307335
Sealfon, C., Verde, L., & Jimenez, R., 2006, *ApJ*, 649, 118

Seljak, U., 2009, *Phys. Rev. Lett.*, 102, 021302
Seljak, U. et al., 2005a, *Phys. Rev. D*, 71, 043511
—, 2005b, *Phys. Rev. D*, 71, 103515
Seo, H.-J., & Eisenstein, D. J., 2003, *ApJ*, 598, 720
—, 2005, *ApJ*, 633, 575
Seo, H.-J., Siegel, E. R., Eisenstein, D. J., & White, M., 2008, *ApJ*, 686, 13
Sheth, R. K., Mo, H. J., & Tormen, G., 2001, *MNRAS*, 323, 1
Silk, J., 1977, *ApJ*, 211, 638
Slosar, A., 2009, *Journal of Cosmology and Astro-Particle Physics*, 3, 4
Spergel, D. N. et al., 2007, *ApJS*, 170, 377
Staniszewski, Z. et al., 2008, ArXiv e-prints, 0810.1578
Sunyaev, R. A., & Zeldovich, I. B., 1980, *ARAA*, 18, 537
Swanson, M. E. C., Tegmark, M., Blanton, M., & Zehavi, I., 2008, *MNRAS*, 385, 1635
Szalay, A. S. et al., 2003, *ApJ*, 591, 1
Tegmark, M., 1997, *Phys. Rev. Lett.*, 79, 3806
Tegmark, M. et al., 2004, *ApJ*, 606, 702
—, 2002, *ApJ*, 571, 191
—, 2006, *Phys. Rev. D*, 74, 123507
Tegmark, M., Hamilton, A. J. S., Strauss, M. A., Vogeley, M. S., & Szalay, A. S., 1998, *ApJ*, 499, 555
Tyson, J. A., 1988, *AJ*, 96, 1
Verde, L., Haiman, Z., & Spergel, D. N., 2002, *ApJ*, 581, 5
Verde, L., Heavens, A. F., & Matarrese, S., 2000, *MNRAS*, 318, 584
Verde, L. et al., 2002, *MNRAS*, 335, 432
Vogeley, M. S., Park, C., Geller, M. J., & Huchra, J. P., 1992, *ApJL*, 391, L5
Vogeley, M. S., & Szalay, A. S., 1996, *ApJ*, 465, 34
Wang, Y., 2006, *ApJ*, 647, 1
Weinberg, D. H., Davé, R., Katz, N., & Hernquist, L., 2004, *ApJ*, 601, 1
White, S. D. M., & Rees, M. J., 1978, *MNRAS*, 183, 341
Willmer, C. N. A. et al., 2006, *ApJ*, 647, 853
Wittman, D. M., Tyson, J. A., Kirkman, D., Dell'Antonio, I., & Bernstein, G., 2000, *Nature*, 405, 143
Yang, X., Mo, H. J., & van den Bosch, F. C., 2008, *ApJ*, 676, 248
Yasuda, N. et al., 2001, *AJ*, 122, 1104
Zaldarriaga, M., & Seljak, U., 2000, *ApJS*, 129, 431
Zehavi, I. et al., 2005, *ApJ*, 630, 1
Zhan, H., 2006, *Journal of Cosmology and Astro-Particle Physics*, 8, 8
Zhan, H., Knox, L., & Tyson, J. A., 2009, *ApJ*, 690, 923
Zhan, H., Knox, L., Tyson, J. A., & Margoniner, V., 2006, *ApJ*, 640, 8